ASCE

Analytical Solution for Inverse Estimation of Groundwater Recharge from Transient Thermal Response in Stratified Media

Vishal Bashist[1]; Ratan Sarmah[2]; and Ickkshaanshu Sonkar[3]

Abstract: Understanding transient heat transport in a layered subsurface media is essential for applications ranging from groundwater recharge estimation to climate signal detection in soil. This study presents an analytical model for 1D transient heat transfer in an *N*-layered soil system, accounting for realistic surface temperature variations induced by diurnal, seasonal, and long-term climatic trends. The governing advection-conduction equation is solved using the generalized integral transform technique, which inherently enforces interfacial continuity of temperature and heat flux across soil layers without the need for recursive matching or numerical Laplace inversion. The proposed solution is validated against existing analytical and numerical models, demonstrating excellent agreement in homogeneous and stratified domains. A local sensitivity analysis identifies key hydrothermal parameters influencing subsurface temperature behavior. The model's inverse capability is further demonstrated through integration with a genetic algorithm, enabling the estimation of vertical water flux from synthetic temperature-depth data and observed field measurements. This work provides the first fully analytical, scalable, and computationally efficient framework for simulating and interpreting subsurface temperature dynamics in stratified systems. Its flexibility and robustness also make it readily applicable to other diffusion-driven transport processes, such as solute and vapor migration in layered geological formations, thereby enhancing its interdisciplinary relevance. **DOI: 10.1061/JHYEFF.HEENG-6716.**

Author keywords: Analytical solution; Heat flow; Layered Soil; Sensitivity analysis; Inverse modelling; Groundwater-surface water exchange.

Introduction

Understanding heat transport in subsurface media is critical due to its wide-ranging applications, including geothermal energy resource assessment (Klepikova et al. 2016), estimation of hydraulic and thermal properties of soil (Kampen et al. 2022; Wagner et al. 2014), estimation of mean water transit time (Bakker et al. 2015; Bekele et al. 2014), and vertical groundwater fluxes quantification (Simon and Bour 2023; Lin et al. 2022; Doro et al. 2015). Heat serves as an effective groundwater tracer due to its ubiquitous presence in the subsurface, nonreactive and noncontaminating nature, and relatively stable thermal properties. Additionally, temperature can be easily monitored using invasive and noninvasive techniques such as thermometers and temperature sensors. This approach is particularly effective in regions with pronounced temperature gradients between the topography and subsurface, which generate distinct temperature-depth profiles suitable for analysis.

Groundwater-induced subsurface heat transfer is often described using the advection–conduction heat transport equation, which can be solved either analytically (Zhou and Wang 2022; Chang and Tsai 2021; Kurylyk and Irvine 2016) or numerically (Liu et al. 2024; LeRoux et al. 2021; Koch et al. 2016). Numerical methods offer the advantage of accommodating complex boundary conditions, heterogeneous media, and nonlinear processes, thereby enabling the construction of models that closely approximate real-world systems. However, the approach is often computationally intensive and may face convergence difficulties during the iterative solution process. In contrast, analytical solutions, though sometimes based on simplifying assumptions, are computationally efficient, free from convergence issues, and can yield accurate temperature-depth predictions under idealized conditions. For these reasons, analytical models remain widely used for predicting subsurface thermal profiles and estimating groundwater flow parameters.

Analytical models of heat transport in subsurface media are typically developed based on a set of fundamental assumptions that simplify the governing equations and make them more tractable (Chang et al. 2023; Kurylyk and Irvine 2016; McCallum et al. 2012). First, heat transfer is assumed to occur exclusively in the vertical direction, with lateral heat flux considered negligible. Second, the subsurface is treated as a homogeneous and isotropic medium, implying uniform thermal and hydraulic properties. Third, groundwater flow is assumed to be steady, with a constant vertical flux throughout the domain. These assumptions, while idealized, are commonly adopted to enable the derivation of analytical solutions that are mathematically manageable and useful for interpreting temperature-depth profiles under simplified field conditions.

Building on the aforementioned assumptions, numerous 1D analytical models have been developed to describe heat transport in the subsurface and simulate temperature-depth profiles. These models are typically classified as either steady-state or transient, depending on whether they account for temporal variations in temperature. Steady-state models are governed by ordinary differential equations and assume that subsurface temperatures remain constant over time. Due to their simplicity, they require only boundary conditions for

[1]Ph.D. Student, Dept. of Civil Engineering, Indian Institute of Technology Ropar, Punjab 140001, India. Email: vishal.23cez0005@iitrpr.ac.in

[2]Assistant Professor, Dept. of Civil Engineering, Indian Institute of Technology Ropar, Punjab 140001, India (corresponding author). Email: ratan@iitrpr.ac.in

[3]Assistant Professor, Dept. of Civil Engineering, Indian Institute of Technology Ropar, Punjab 140001, India. Email: ickkshaanshu@iitrpr.ac.in

Note. This manuscript was submitted on June 29, 2025; approved on October 17, 2025; published online on December 29, 2025. Discussion period open until May 29, 2026; separate discussions must be submitted for individual papers. This paper is part of the ***Journal of Hydrologic Engineering***, © ASCE, ISSN 1084-0699.

solution and are computationally efficient. For instance, Bredehoeft and Papaopulos (1965) introduced a model incorporating a constant temperature at the lower boundary, while Harris and Chapman (1995) proposed an alternative model that applied a constant heat flux at depth. Shan and Bodvarsson (2004) extended steady-state modeling to multilayered media by incorporating variations in thermal diffusivity across different strata. However, a key limitation of steady-state models is their inability to capture time-dependent changes in surface temperature, such as those induced by diurnal, seasonal, or long-term climatic fluctuations (Bense and Kurylyk 2017; Irvine et al. 2016).

Since temperature-depth profiles are strongly influenced by surface temperature variations, driven by natural processes and anthropogenic activities, transient models are required for more accurate characterization. Natural variations typically occur over longer timescales (e.g., daily, seasonal, or annual cycles), whereas human-induced changes can result in rapid fluctuations on the scale of minutes to hours (Kurylyk et al. 2018; Taniguchi et al. 1999). Transient models account for these dynamics and are governed by partial differential equations, making them inherently more complex than their steady-state counterparts. In addition to boundary conditions, these models require initial temperature distributions for prediction of subsurface thermal regimes. They often assume a semi-infinite domain to simplify boundary effects at depth. Various forms of transient analytical solutions have been developed to account for different surface temperature input patterns. Stallman (1965) formulated a model assuming sinusoidal surface temperature variations. Kurylyk and Macquarrie (2013) analyzed the influence of exponential surface warming, while Taniguchi et al. (1999) studied linear temperature increases. Step changes in surface temperature were modeled by Kurylyk and Irvine (2016). More recently, Chang and Tsai (2021) introduced a generalized transient model capable of accommodating arbitrary surface temperature changes, with the added realism of finite subsurface thickness. These developments highlight the increasing sophistication of analytical approaches in capturing the temporal complexity of subsurface heat transport.

Despite these advancements, steady-state and transient models exhibit certain limitations. In steady-state frameworks, bottom boundary conditions are often restricted to either prescribed temperatures or constant heat fluxes, with the convective boundary condition serving as a generalized alternative. Transient models, while more realistic, frequently rely on the semi-infinite domain assumption and predefined surface forcing functions. Although the generalized model by Chang and Tsai (2021) mitigates some of these constraints, most transient models also assume homogeneous soil properties. In reality, the subsurface is typically stratified, comprising multiple soil layers with distinct physical properties (Sarmah et al. 2022). To address this, Shi and Wang (2023) developed a semianalytical transient model for a three-layered soil system. While effective for limited-layer configurations, extending their method to a system with an arbitrary number of layers introduces significant computational complexity. This is due to the need for explicit interface matching conditions and the growing number of coefficients as the layer count increases. The authors' solution approach also involves Laplace transformation to manage the temporal derivative in the governing equation, requiring numerical inversion to retrieve the solution in the original time domain, an added computational burden. These challenges highlight the pressing need for a more generalized, scalable analytical framework capable of efficiently addressing transient heat transfer in N-layered stratified soils. Such a model would enhance the feasibility and practicality of simulating subsurface thermal regimes and could be readily adapted to other transport processes governed by similar partial differential equations, such as those describing advection-dispersion phenomena.

In this study, an analytical 1D transient heat transfer model is developed for an N-layered soil system, extending the steady-state solution of Shan and Bodvarsson (2004) by incorporating realistic surface temperature forcing that accounts for diurnal, seasonal, and long-term climate-induced temperature variations. The surface boundary condition is represented by a combined sinusoidal function to simulate daily and seasonal cycles and a linear trend to capture decadal-scale climate change, while the bottom boundary is assumed to have a constant temperature. The generalized integral transform technique (GITT) is used to solve the governing equation, implicitly enforcing interface continuity of temperature and heat flux without requiring explicit interface condition handling. This enables scalable modeling for arbitrarily stratified soils, overcoming the complexity barrier associated with increasing the number of layers.

To the best of our knowledge, this is the first fully analytical transient model for multilayered subsurface systems that combines computational simplicity with broad applicability. Unlike traditional approaches that rely on recursive or numerical Laplace-inversion-based solutions, the present method preserves analytical tractability while offering high flexibility in boundary and initial conditions. The analytical solution is verified against finite element simulations in COMSOL Multiphysics. A key advancement of this work lies in its inverse modeling capability, which enables the estimation of vertical groundwater flux, directly from observed layered temperature-depth profile data. Traditionally, estimating vertical water flux through an unsaturated zone requires solving Richards' equation with appropriate boundary conditions, an inherently complex task due to the nonlinear nature of the soil–water characteristic curve (Kumar et al. 2024). Even numerical solutions often encounter convergence issues (Farthing and Ogden 2017). The proposed method circumvents these challenges by enabling indirect estimation of flux without the need for detailed soil hydraulic properties or boundary condition specifications. This is achieved through integration with MATLAB's genetic algorithm toolbox, allowing for efficient parameter estimation even in complex, layered soil systems. Additionally, a local sensitivity analysis is performed to assess the influence of input parameters on subsurface thermal dynamics, providing insight into the dominant controls governing heat transport in layered geologic media.

The framework developed in this study has broad practical relevance for field-scale investigations such as groundwater recharge estimation and soil temperature forecasting for agricultural planning. By enabling the noninvasive characterization of subsurface hydrological conditions using readily obtainable thermal data, the proposed methodology serves as a powerful tool for environmental monitoring and hydrogeological analysis. The integrated framework, comprising fully analytical modeling, inverse parameter estimation via optimization, and local sensitivity analysis, presents a computationally efficient, scalable, and field-relevant solution for simulating transient heat transport in stratified media. Further, the structure of the model is readily extensible to other diffusion-dominated transport phenomena, such as solute and vapor migration in layered geological formations, enhancing its interdisciplinary applicability.

Problem Statement and Mathematical Model

Fig. 1 illustrates the conceptual model developed for this study, depicting 1D heat transport in an N-layer subsurface system, each exhibiting distinct hydrogeological characteristics. The water and heat transport are treated as 1D by neglecting the horizontal water flow in the subsurface media. Water movement within the porous

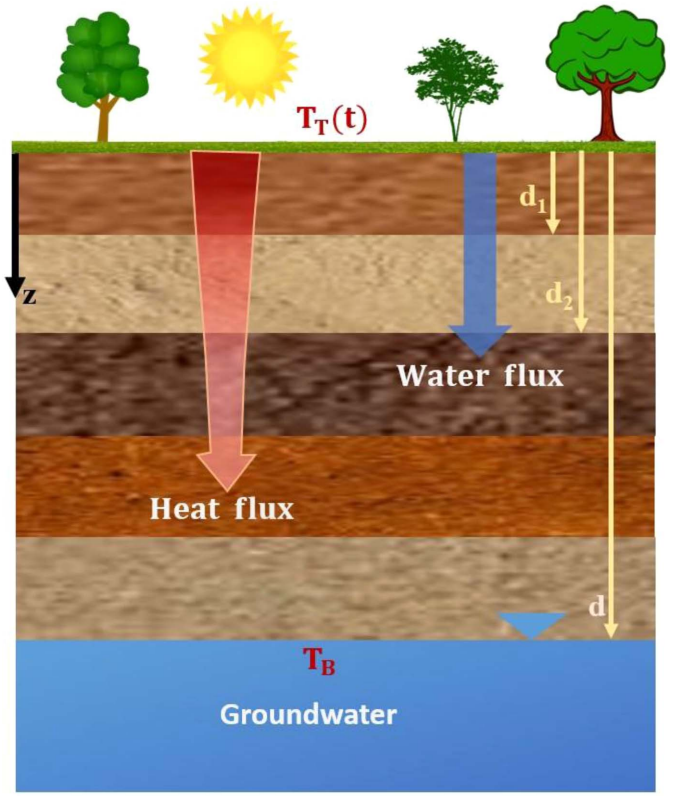

Fig. 1. Schematic representation of 1D heat transport in a stratified subsurface media.

media is considered to be in a steady-state, representing a long-term average behavior of subsurface water flow dynamics. Under a 1D steady-state flow condition, the water flux remains constant throughout the domain, regardless of whether the medium is saturated or unsaturated. Heat enters the flow domain due to fluctuations in the ground surface temperature, which vary across three temporal scales: diurnal; seasonal; and decadal. A constant temperature is maintained at the water table located at the bottom of the flow domain. The origin of the coordinate system is set at the soil surface, measuring positive values in the downward direction.

Mathematical Formulation

Heat flow through subsurface media is driven by the combined effects of conduction through soil and advection by water flow within the media. As a result of temperature fluctuations at the soil surface and the conduction-advection capacity of the subsurface media, a continuous spatiotemporal temperature profile develops within the subsurface region. The governing equation that describes the spatiotemporal variation in temperature within a layered subsurface media is given by Suzuki (1960)

$$\frac{\partial}{\partial z}\left(\lambda_i \frac{\partial T}{\partial z}\right) - qc_w\rho_w \frac{\partial T}{\partial z} = c_i\rho_i \frac{\partial T}{\partial t}, \quad (d_{i-1} \le z \le d_i) \tag{1}$$

where T = the subsurface temperature (°C) profile; z = the depth below the ground surface (m); λ_i = thermal conductivity of the ith soil layer (W/m/°C); q = constant vertical water flux (m/s), $c_w\rho_w$ = the volumetric heat capacity of water (J/m^3/°C); $c_i\rho_i$ = the volumetric heat capacity of the ith soil layer (J/m^3/°C); and d_i = the interface depth between the ith and $(i+1)$th soil layers, measured from the top surface. Since the flow domain consists of multiple vertically stacked layers, temperature and heat flux conservation are inevitable. Therefore, the following interface conditions are prescribed at the junction of the soil layers

$$T(d_i^-, t) = T(d_i^+, t) \tag{2}$$

and

$$\lambda_i \frac{\partial T(d_i^-, t)}{\partial z} - qc_w\rho_w T(d_i^-, t) = \lambda_{i+1} \frac{\partial T(d_i^+, t)}{\partial z} - qc_w\rho_w T(d_i^+, t) \tag{3}$$

As a consequence of applying Eqs. (2) and (3), the latter transforms into

$$\lambda_i \frac{\partial T(d_i^-, t)}{\partial z} = \lambda_{i+1} \frac{\partial T(d_i^+, t)}{\partial z} \tag{4}$$

At the soil surface, a transient heat boundary condition is applied to capture the combined effects of temperature variations caused by diurnal, seasonal, and decadal fluctuations, expressed as

$$T(0,t) = T_T(t) = T_{av} + C_0 t + A_0 \sin\left(\frac{2\pi}{P_s} t\right) + B_0 \sin\left(\frac{2\pi}{P_d} t\right) \tag{5}$$

where T_{av} = the reference average surface temperature (°C); C_0 = the slope of decadal temperature rise due to climate change (°C/decade); A_0 = the amplitude of seasonal temperature variation (°C); P_s = the period of the seasonal variation, typically taken as 365 days; B_0 = the amplitude of the diurnal variation (°C); and P_d = the period of the diurnal variation, typically taken as one day. The bottom end of the flow domain is positioned exactly at the water table and is maintained at a constant temperature boundary condition, expressed as

$$T(d,t) = T_B \tag{6}$$

Additionally, Eq. (1) is solved subjected to an initial temperature profile, as given by

$$T(z,0) = T_r(z) \tag{7}$$

In this study, $T_r(z)$ is taken as the steady-state solution of Eq. (1) subjected to a constant soil surface temperature T_{av}, obtained by setting $t = 0$ in Eq. (5).

Next, we transformed the governing equation and its associated parameters into a dimensionless form, defined by

$$\bar{T} = \frac{T}{T_{av}}, \qquad \bar{z} = \frac{z}{d}, \qquad \bar{t} = \frac{t}{P_s},$$
$$\omega_i = \frac{\lambda_i}{qc_w\rho_w d} \quad \text{and} \quad \sigma_i = \frac{c_i\rho_i d}{qc_w\rho_w P_s} \tag{8}$$

As a consequence of the transformations defined here, the governing equation [Eq. (1)] and the associated boundary conditions [Eqs. (2), (4)–(6)] are transformed into

$$\frac{\partial}{\partial \bar{z}}\left(\omega_i \frac{\partial \bar{T}}{\partial \bar{z}}\right) - \frac{\partial \bar{T}}{\partial \bar{z}} = \sigma_i \frac{\partial \bar{T}}{\partial \bar{t}} \quad (\bar{d}_{i-1} \le \bar{z} \le \bar{d}_i) \tag{9}$$

and

$$\bar{T}(\bar{d}_i^-, \bar{t}) = \bar{T}(\bar{d}_i^+, \bar{t}) \tag{10}$$

$$\omega_i \frac{\partial \bar{T}(\bar{d}_i^-, \bar{t})}{\partial \bar{z}} = \omega_{i+1} \frac{\partial \bar{T}(\bar{d}_i^+, \bar{t})}{\partial \bar{z}} \tag{11}$$

$$\bar{T}(0,\bar{t}) = \bar{T}_T(\bar{t}) = 1 + \bar{C}_0\bar{t} + \bar{A}_0\sin(2\pi\bar{t}) + \bar{B}_0\sin\left(\frac{2\pi P_s}{P_d}\bar{t}\right) \quad (12)$$

$$\bar{T}(\bar{d},\bar{t}) = \bar{T}_B \quad (13)$$

$$\bar{T}(\bar{z},0) = \bar{T}_r(\bar{z}) \quad (14)$$

where $\bar{d}_i = (d_i/d)$, $\bar{C}_0 = (C_0/T_{av})$, $\bar{A}_0 = (A_0/T_{av})$, $\bar{B}_0 = (B_0/T_{av})$, and $\bar{T}_r = (T_r/T_{av})$.

Eq. (9) represents the nondimensional form of the governing differential equation for 1D transient heat transfer in a layered subsurface media.

Analytical Solution

To derive the desired analytical solution, the original mathematical model is decomposed into two separate models using the principle of superposition. The first model ignores the volumetric heat storage effect but incorporates the unsteady temperature boundary, while the second model accounts for the aquifer's heat storage with a zero-temperature boundary at the soil surface. Mathematically, this can be expressed as

$$\bar{T}(\bar{z},\bar{t}) = \bar{T}_{st}(\bar{z},\bar{t}) + \bar{U}(\bar{z},\bar{t}) \quad (15)$$

where $\bar{T}_{st}(\bar{z},\bar{t})$ = the solution of Eq. (9), which neglects the aquifer's heat storage effect ($\sigma_i = 0$) but accounts for the transient heat boundary at the soil surface as defined by the boundary condition in Eq. (12). In other words, $\bar{T}_{st}(\bar{z},\bar{t})$ represents the steady-state part of Eq. (9) with an unsteady temperature boundary $\bar{T}_T(\bar{t})$ at the top surface. On the other hand, $\bar{U}(\bar{z},\bar{t})$ is the solution of Eq. (9), which incorporates the influence of the aquifer heat storage (σ_i) while neglecting the temperature variation at the surface [$\bar{T}_T(\bar{t}) = 0$]. Substituting Eq. (15) along with definitions into Eq. (9), we obtain the governing equation for $\bar{T}_{st}$ in the form of

$$\frac{\partial}{\partial\bar{z}}\left(\omega_i\frac{\partial\bar{T}_{st}}{\partial\bar{z}}\right) - \frac{\partial\bar{T}_{st}}{\partial\bar{t}} = 0 \quad (\bar{d}_{i-1} \le \bar{z} \le \bar{d}_i) \quad (16)$$

subjected to the boundary conditions

$$\bar{T}_{st}(\bar{d}_i^-,\bar{t}) = \bar{T}_{st}(\bar{d}_i^+,\bar{t}) \quad (17)$$

$$\omega_i\frac{\partial\bar{T}_{st}(\bar{d}_i^-,\bar{t})}{\partial\bar{z}} = \omega_{i+1}\frac{\partial\bar{T}_{st}(\bar{d}_i^+,\bar{t})}{\partial\bar{z}} \quad (18)$$

$$\bar{T}_{st}(0,\bar{t}) = \bar{T}_T(\bar{t}) = 1 + \bar{C}_0\bar{t} + \bar{A}_0\sin(2\pi\bar{t}) + \bar{B}_0\sin\left(\frac{2\pi P_s}{P_d}\bar{t}\right) \quad (19)$$

$$\bar{T}_{st}(\bar{d},\bar{t}) = \bar{T}_B \quad (20)$$

The analytical expression for $\bar{T}_{st}$ is derived by solving Eq. (16) in conjunction with Eqs. (17)–(20). The solutions are derived individually for each soil layer and are linked through interfacial temperature and heat flux continuity conditions. The detailed derivation of $\bar{T}_{st}(z,t)$ for an N-layer system is presented in Appendix I. Here, we present the solution for a three-layer soil system, expressed as

$$\bar{T}_{st1}(\bar{z},\bar{t}) = \frac{\bar{T}_T\exp(\alpha) - \bar{T}_B}{\exp(\alpha) - 1} + \frac{\bar{T}_B - \bar{T}_T}{\exp(\alpha) - 1}\exp\left(\frac{\bar{z}}{\omega_1}\right), \quad (0 \le \bar{z} \le \bar{d}_1) \quad (21)$$

$$\bar{T}_{st2}(\bar{z},\bar{t}) = \frac{\bar{T}_T\exp(\alpha) - \bar{T}_B}{\exp(\alpha) - 1} + \frac{\bar{T}_B - \bar{T}_T}{\exp(\alpha) - 1} \times \exp\left[\bar{d}_1\left(\frac{1}{\omega_1} - \frac{1}{\omega_2}\right) + \frac{\bar{z}}{\omega_2}\right], \quad (\bar{d}_1 \le \bar{z} \le \bar{d}_2) \quad (22)$$

and

$$\bar{T}_{st3}(\bar{z},\bar{t}) = \frac{\bar{T}_T\exp(\alpha) - \bar{T}_B}{\exp(\alpha) - 1} + \frac{\bar{T}_B - \bar{T}_T}{\exp(\alpha) - 1}\exp\left[\bar{d}_1\left(\frac{1}{\omega_1} - \frac{1}{\omega_2}\right) + \bar{d}_2\left(\frac{1}{\omega_2} - \frac{1}{\omega_3}\right) + \frac{\bar{z}}{\omega_3}\right] \quad (\bar{d}_2 \le \bar{z} \le \bar{d}) \quad (23)$$

where

$$\alpha = \bar{d}_1\left(\frac{1}{\omega_1} - \frac{1}{\omega_2}\right) + \bar{d}_2\left(\frac{1}{\omega_2} - \frac{1}{\omega_3}\right) + \left(\frac{\bar{d}}{\omega_3}\right) \quad (24)$$

The next step involves developing the analytical expression for the transient model $\bar{U}(\bar{z},\bar{t})$ while considering homogeneous temperature profiles at the end boundaries. This is achieved by reformulating the governing equation [Eq. (9)] in terms of $\bar{U}(\bar{z},\bar{t})$ using Eq. (15), given by

$$\frac{\partial}{\partial\bar{z}}\left(\omega_i\frac{\partial\bar{U}}{\partial\bar{z}}\right) - \frac{\partial\bar{U}}{\partial\bar{z}} = \sigma_i\left(\frac{\partial\bar{T}_{st}}{\partial\bar{t}} + \frac{\partial\bar{U}}{\partial\bar{t}}\right) \quad (\bar{d}_{i-1} \le \bar{z} \le \bar{d}_i) \quad (25)$$

subjected to the initial and boundary conditions

$$\bar{U}(\bar{d}_i^-,\bar{t}) = \bar{U}(\bar{d}_i^+,\bar{t}) \quad (26)$$

$$\omega_i\frac{\partial\bar{U}(\bar{d}_i^-,\bar{t})}{\partial\bar{z}} = \omega_{i+1}\frac{\partial\bar{U}(\bar{d}_i^+,\bar{t})}{\partial\bar{z}} \quad (27)$$

$$\bar{U}(0,\bar{t}) = 0 \quad (28)$$

$$\bar{U}(\bar{d},\bar{t}) = 0 \quad (29)$$

$$\bar{U}(\bar{z},0) = \bar{T}_r(\bar{z}) - \bar{T}_{st}(\bar{z},0) \quad (30)$$

The transient component of the analytical model $\bar{U}(\bar{z},\bar{t})$ is derived using a different approach than that used for the quasisteady solution $\bar{T}_{st}(\bar{z},\bar{t})$. Unlike the approach used for $\bar{T}_{st}$, the domain is not divided; instead, a single mathematical expression is derived, which remains valid across the entire domain while satisfying all specified boundary conditions. In other words, the interface conditions at the junction between layers are inherently integrated into the solution methodology without partitioning the domain. Alternatively, the same problem can be solved separately for individual layers and then explicitly linked by enforcing interface conditions. However, this approach becomes significantly complex, as it involves an iterative procedure to determine the eigenvalues and coefficients for each layer (Aryeni and Ginting 2022; Liu and Si 2008; Sarmah et al. 2022), with the complexity further increasing as the number of layers in the flow domain grows. Therefore, in this study, a single mathematical expression is derived for the transient solution, valid across the entire domain, implicitly incorporating the layer interface conditions, following the procedure outlined by Deng et al. (2014).

To define the flow valid for the entire flow domain, we will redefine ω and σ as a function of $\bar{z}$, in the form

$$\omega(\bar{z}) = \begin{cases} \omega_1 & 0 \le \bar{z} \le \bar{d}_1 \\ \omega_2 & \bar{d}_1 \le \bar{z} \le \bar{d}_2 \\ . & . \\ . & . \\ . & . \\ \omega_N & \bar{d}_{N-1} \le \bar{z} \le \bar{d} \end{cases} \tag{31}$$

and

$$\sigma(\bar{z}) = \begin{cases} \sigma_1 & 0 \le \bar{z} \le \bar{d}_1 \\ \sigma_2 & \bar{d}_1 \le \bar{z} \le \bar{d}_2 \\ . & . \\ . & . \\ . & . \\ \sigma_N & \bar{d}_{N-1} \le \bar{z} \le \bar{d} \end{cases} \tag{32}$$

Thus, Eq. (25) can be rewritten for the entire domain, incorporating the defined relations, as follows:

$$\frac{\partial}{\partial \bar{z}}\left[\omega(\bar{z})\frac{\partial \bar{U}}{\partial \bar{z}}\right] - \frac{\partial \bar{U}}{\partial \bar{z}} = \sigma(\bar{z})\left(\frac{\partial \bar{T}_{st}}{\partial \bar{t}} + \frac{\partial \bar{U}}{\partial \bar{t}}\right) \quad (0 \le \bar{z} \le \bar{d}) \tag{33}$$

subjected to the following initial and boundary conditions defined in Eqs. (28)–(30).

The dimensionless heat flux at any location within the flow domain can be expressed using Eq. (33) as

$$\bar{J} = \bar{U} - \omega(\bar{z})\frac{\partial \bar{U}}{\partial \bar{z}} \tag{34}$$

Since there is no accumulation or degradation (sink/source) of temperature in the interface between the soil layers, the dimensionless heat flux $\bar{J}$ is equal from either side of the interface, i.e.,

$$\bar{J}(\bar{d}_i^-, \bar{t}) = \bar{J}(\bar{d}_i^+, \bar{t}) \tag{35}$$

By incorporating Eqs. (31) and (32) into Eq. (34), it becomes evident that Eq. (35) is an exact representation of the actual interface condition given in Eq. (27). Thus, by solving Eq. (33) alongside the variables defined in Eqs. (31) and (32), the interface conditions [Eqs. (26) and (27)] are implicitly accounted for in this study without the need to explicitly invoke them.

The analytical expression for $\bar{U}(\bar{z}, \bar{t})$ is obtained by solving Eq. (33) using GITT (Cotta et al. 2020; Deng et al. 2014; Mikhailov and Ozisik 1984) while accounting for the initial and boundary conditions specified in Eqs. (28)–(30). The mathematical procedures used in the present study follow a similar approach to that of Deng et al. (2014), as detailed in Appendix II. A detailed comparison of these two approaches based on accuracy is presented in the section "Performance Comparison between the Proposed Analytical Model and the Deng et al. (2014) Model." Using the orthogonality property of the Eigenfunctions, the analytical expression for $\bar{U}(\bar{z}, \bar{t})$ is formulated in the form

$$\bar{U}(\bar{z}, \bar{t}) = \sum_{m=1}^{M} \tau_m(\bar{t}) \frac{\sin(\frac{m\pi}{\bar{d}}\bar{z})}{(\beta_m)^{1/2}} \tag{36}$$

where

$$\beta_m = \int_0^{\bar{d}} \sin^2\left(\frac{m\pi}{\bar{d}}\bar{z}\right) d\bar{z} = \frac{\bar{d}}{2} \tag{37}$$

To determine the unknown transient function $\tau_m(\bar{t})$ defined in Eq. (36), we applied the integral operator

$$\frac{1}{(\beta_m)^{1/2}} \int_0^{\bar{d}} (\cdot) \sin\left(\frac{m\pi}{\bar{d}}\bar{z}\right) d\bar{z}$$

to Eq. (33). This leads to formation of a set of ordinary differential equations for $\tau_m(\bar{t})$ with respect to $\bar{t}$, as expressed by

$$\mathbf{D}\frac{d\boldsymbol{\tau}}{d\bar{t}} + \mathbf{E}\boldsymbol{\tau}(\bar{t}) = \mathbf{F}(\bar{t}) \tag{38}$$

The expressions for $\mathbf{D}$, $\mathbf{E}$, and $\mathbf{F}(\bar{t})$ can be found in Eqs. (66), (73), and (76), respectively, in Appendix II. The solution of the equation provides the expression for $\boldsymbol{\tau}(\bar{t})$, which, then substituted into Eq. (36), ultimately determines the expression for $\bar{U}(\bar{z}, \bar{t})$. Upon solving Eq. (38), $\boldsymbol{\tau}(\bar{t})$ is obtained as

$$\boldsymbol{\tau}(\bar{t}) = \exp(-\mathbf{D}^{-1}\mathbf{E}\bar{t})\boldsymbol{\tau}(0) + \exp(-\mathbf{D}^{-1}\mathbf{E}\bar{t}) \int_0^{\bar{t}} \exp(\mathbf{D}^{-1}\mathbf{E}\bar{t})\mathbf{D}^{-1}\mathbf{F}(\bar{t})d\bar{t} \tag{39}$$

Appendix II provides a detailed breakdown of the intermediate steps of this mathematical derivation.

Sensitivity Analysis

In this study, a local sensitivity analysis is performed to assess the impact of flow parameters on the dimensionless subsurface temperature-depth profile. This analysis quantifies the responsiveness of the model output to small perturbations in input parameters. The normalized sensitivity coefficients corresponding to each geothermal parameter in the flow model are represented by

$$S_i = \frac{\partial X}{\partial P_i}\frac{P_i}{X} \tag{40}$$

where P_i = the magnitude of the ith input parameter; and X = the model output. The central total relative sensitivity (CTRS) index corresponding to Eq. (40) can be expressed as (Rezaei et al. 2016)

$$CTRS = \frac{X(P_i + \Delta P_i) - X(P_i - \Delta P_i)}{2p_f P_i}\frac{P_i}{X} \tag{41}$$

where p_f = the perturbation factor, which is set to 5% in this study.

Field Data Interpretation

To evaluate the field applicability of the developed model, we employed streambed temperature data collected by the U.S. Geological Survey to estimate streambed flux in a layered system. The data set consists of temperature measurements obtained in 2016, with the first complete record beginning on ordinal day 158, as reported by Kurylyk et al. (2017b). The streambed was conceptualized as a two-layer profile comprising a surficial organic mud layer underlain by sand. The suitability of the developed model for this data set was supported by the assumptions of steady water flux, uniform intralayer thermal properties, and local thermal equilibrium between soil and water. Under these assumptions, the model is valid for saturated and unsaturated soils.

To ensure compatibility between the field data and the developed model, the boundary and initial conditions were defined in accordance with site observations. The proposed solution is capable of simulating heat transport in porous media under a wide range of temporal boundary conditions, from diurnal cycles to decadal climate variations. However, as the available data set spans a 24 h period, the top boundary condition must be adapted to capture short-term fluctuation. Accordingly, the top boundary condition was modified following Eq. (12), expressed as

$$\bar{T}(0,\bar{t}) = \bar{T}_T(\bar{t}) = \bar{T}_1 + \left(\frac{\bar{T}_2 - \bar{T}_1}{\bar{T}_P}\right)\bar{t} + \sum_{m=1}^{\infty} \bar{A}_m \sin\left(\frac{m\pi}{\bar{T}_P}\bar{t}\right) \quad (42)$$

where $\bar{T}_1$ and $\bar{T}_2$ = the dimensionless temperatures corresponding to the first and last data points of the observed boundary temperature, which corresponds to $\bar{t} = 0$ and $\bar{t} = \bar{T}_P$, respectively, where $\bar{T}_P = (P_d/P_s)$ and $P_d = 0.98$ days, denotes the dimensionless period.

The amplitude for the mth sinusoidal term in Eq. (42) is given by

$$\bar{A}_m = \frac{2}{\bar{T}_P}\int_0^{\bar{T}_P}\left[\bar{T}_T(\bar{t}) - \bar{T}_1 - \left(\frac{\bar{T}_2 - \bar{T}_1}{\bar{T}_P}\right)\bar{t}\right]\sin\left(\frac{m\pi}{\bar{T}_P}\bar{t}\right)d\bar{t} \quad (43)$$

where $\bar{T}_T(\bar{t})$ = the observed boundary temperature at discrete time points. Consequently, the integral term

$$\int_0^{\bar{T}_P} \bar{T}_T(\bar{t})\sin\left(\frac{m\pi}{\bar{T}_P}\bar{t}\right)d\bar{t}$$

was evaluated numerically using the trapezoidal rule (Scarborough 1966), while the remaining components of Eq. (43) were computed analytically.

The bottom boundary condition was prescribed as the temporal average of the dimensionless temperature at the lower edge, yielding $\bar{T}_B = 0.4153$. The initial condition, $\bar{T}_r(\bar{z})$, for the heat flow problem was determined by applying the least-squares method to fit straight-line segments for each layer using the observed temperature data at the initial reference time ($\bar{t} = 0$). The fitted initial temperature profile was expressed as

$$\bar{T}_r(\bar{z}) = \begin{cases} c_1 + c_2 z, & 0 < \bar{z} < \bar{d}_1 \\ c_1 + c_2 z, & \bar{d}_1 < \bar{z} < \bar{d} \end{cases} \quad (44)$$

The spatio-temporal variation of dimensionless temperature subjected to the initial and boundary conditions discussed here was simulated using the analytical solution given in Eq. (15). The quasi-steady response under nonhomogenous boundary, $\bar{T}_{st}(\bar{z},\bar{t})$, was evaluated using Eqs. (21)–(23), whereas the transient response with homogenous boundary, $\bar{U}(\bar{z},\bar{t})$, was obtained from Eq. (36), with the associated transient coefficient $\tau_m(\bar{t})$ determined from Eq. (39). The transient coefficient corresponding to initial time $\bar{t} = 0$ was evaluated using Eq. (80), expressed as

$$\bar{U}(\bar{z},0) = \sum_{m=1}^{M} \tau_m(0)\frac{\sin(N_m\bar{z})}{(\beta_m)^{1/2}} = \bar{T}_r(\bar{z}) - \bar{T}_{st}(\bar{z},0) \quad (45)$$

where $\bar{T}_r(\bar{z})$ = the initial condition of the heat flow problem as defined in Eq. (44); and $\bar{T}_{st}(\bar{z},0)$ = the quasi-steady temperature profile, obtained by substituting $\bar{t} = 0$ into Eqs. (21)–(23).

Applying the Fourier series expansion in the domain $0 < \bar{z} < \bar{d}$ to Eq. (45) yields

$$\tau_m(0) = \frac{1}{(\beta_m)^{1/2}}\int_0^{\bar{d}}[\bar{T}_r(\bar{z}) - \bar{T}_{st}(\bar{z},0)]\sin(N_m\bar{z})d\bar{z} \quad (46)$$

Results and Discussion

This section is divided into two subsections. Section "Validation of the Proposed Solution," presents a comparative analysis and validation of the proposed model with the existing analytical and numerical models. Section "Discussion," focuses to examine the variations in the spatio-temporal temperature profile in response to diurnal, seasonal, and decadal temperature fluctuations. Additionally, a local sensitivity analysis is conducted to assess the influence of soil hydrothermal parameters on the computed subsurface temperature profile. Further, an optimization study is conducted to demonstrate the field applicability of the proposed solution in determining inverse water flux based on observed temperature data. The geothermal and other model parameter values used in this study are listed in Table 1 to avoid repetition, unless specified otherwise for particular cases. These values fall within the range observed in real field conditions and are sourced from previous research studies (Chang et al. 2023; Kothawale and Singh 2017; Kumar et al. 2023; Singh et al. 2024).

Table 1. Model parameter values used in the analysis

Parameter	Values
Thermal conductivity of sand	2.2 W/m/°C
Thermal conductivity of silt	1.89 W/m/°C
Thermal conductivity of clay	1.58 W/m/°C
Volumetric heat capacity of sand	2.96×10^6 J/m^3/°C
Volumetric heat capacity of silt	3.03×10^6 J/m^3/°C
Volumetric heat capacity of clay	3.1×10^6 J/m^3/°C
Volumetric heat capacity of water	4.18×10^6 J/m^3/°C
Reference average temperature (T_{av})	25°C
Temperature in the bottom boundary (T_B)	22°C
Amplitude of seasonal temperature variation (A_0)	12°C
Amplitude of the diurnal variation (B_0)	6°C
Slope of decadal temperature rise (C_0)	0.2°C/decade
Depth of the top soil layer from the top surface (d_1)	6 m
Depth of the middle soil layer from the top surface (d_2)	9 m
Total depth of the soil column (d)	15 m
Period of the seasonal variation (P_s)	365 days
Period of the diurnal variation (P_d)	24 h
Vertical water flux (q)	0.33 m/year

Validation of the Proposed Solution

The accuracy of the proposed model is verified by comparing it with existing analytical models for a simplified flow scenario. The first analytical comparison is conducted using the solution provided by Taniguchi et al. (1999), which assumes uniform thermohydrogeological properties throughout the flow domain, a time-dependent temperature boundary at the soil surface with a linear variation, and an infinitely deep flow field. The proposed analytical solution is reduced to Taniguchi et al.'s (1999) model by removing variations in the thermal and hydrogeological properties of the soil in each layer and assuming uniform thermal conductivity and volumetric heat capacity. This is done by assigning a constant thermal conductivity and volumetric heat capacity coefficient, such that $\lambda_i = \lambda_{i+1} = \lambda$ and $c_i\rho_i = c_{i+1}\rho_{i+1} = c\rho$. A linear time-dependent temperature variation at the top surface is introduced into our model by setting $A_0 = B_0 = 0$. Also, a uniform sandy soil is considered to represent homogeneous conditions, with the corresponding thermal and hydrogeological properties taken from Table 1. Since the solution proposed by Taniguchi et al. (1999) applies to an infinite domain, we set the total depth d to 100 m. However, the temperature profile was compared only during the early stages of the simulation, before the temperature rise at the boundary affected the bottom boundary. For comparison, we analyzed the dimensionless temperature profiles of the proposed model and the model by Taniguchi et al. (1999) at four different dimensionless time points, i.e., $\bar{t} = 5$, 10, 15, and 20.

Fig. 2 shows a close agreement between the dimensionless temperature profiles obtained from the proposed analytical model, which assumes uniform thermal and hydrogeological properties, and the analytical model by Taniguchi et al. (1999) across the entire domain.

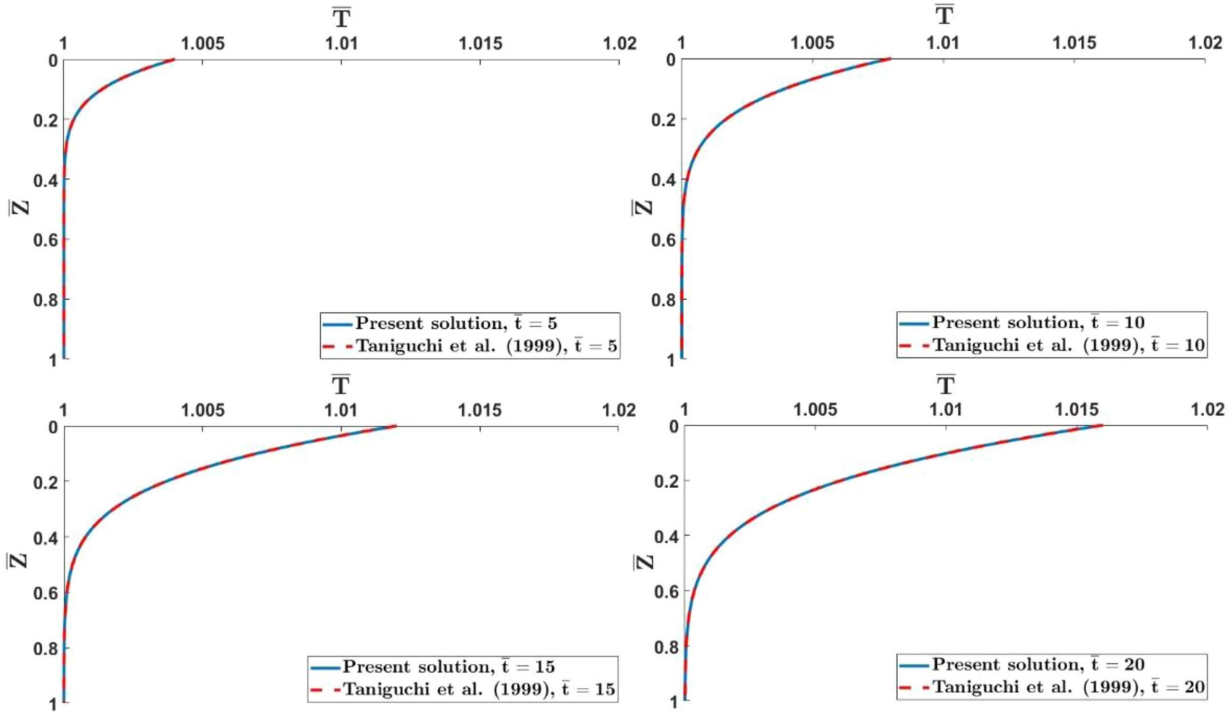

Fig. 2. Subsurface dimensionless temperature-depth profiles predicted by the proposed solution and the solution by Taniguchi et al. (1999) for a homogeneous soil column under a linearly increasing top surface temperature boundary.

The second analytical comparison is conducted between the proposed model and the model presented by Kurylyk et al. (2017b) under steady-state flow conditions. The comparative analysis is conducted for a three-layered soil system under a constant temperature boundary at the soil surface. The top layer consists of silt, the bottom layer is composed of sand, and the middle layer, made of clay, is sandwiched between them. The thermal and hydrogeological property values for these soil layers are obtained from Table 1. The constant temperature boundary at the soil surface is enforced by setting $A_0 = B_0 = C_0 = 0$. To achieve a steady-state solution, the simulation in the proposed model is conducted with $t \to \infty$.

Fig. 3 shows strong agreement between the dimensionless temperature profiles from the proposed analytical model and the analytical model by Kurylyk et al. (2017b) across the entire domain. It is important to note that, at the interfaces between adjacent soil layers (at $\bar{d}_1 = 0.4$ and $\bar{d}_2 = 0.6$), a slight kink (a change in slope) appears in the temperature profile due to the discontinuity in the thermal properties of the soil at these locations. However, the extent of the kink in the temperature profile depends on the ratio of the thermal properties between the adjacent soil layers.

A finite element model was developed using COMSOL Multiphysics to numerically compare the results obtained from the proposed analytical solution. The simulation was implemented through the mathematics interface, which facilitates the incorporation of user-defined partial differential equations, algebraic equations, and spatially invariant expressions. The governing flow problem, as illustrated in Fig. 1, was modeled by applying the boundary conditions specified in Eqs. (19) and (20) at the top and bottom boundaries, respectively. For spatial discretization, the model utilized COMSOL's default linear Lagrange elements. A fine computational mesh with a grid size of 0.002 was employed across the domain to ensure spatial accuracy, and a time step of 0.01 was adopted to maintain numerical stability and convergence.

Fig. 4 illustrates good agreement between the dimensionless temperature profiles obtained from the proposed analytical model and the COMSOL simulation in a three-layered soil system, accounting for transient heat flow under a fluctuating temperature boundary at the surfaced. The comparison plots are presented for four dimensionless time snapshots, i.e., $\bar{t} = 0.25$, 0.5, 0.75, and 1. The figure clearly shows that the temperature profile exhibits a kink at the interface between the soil layers at all time instances. Additionally, the maximum error between the proposed solution and the numerical solution is found to be 0.0038, with an RMSE of 0.00024.

Discussion

Assessment of the Impact of Seasonal, Diurnal, and Decadal Temperature Variations on Heat Transfer in a Layered Medium

The proposed solution is employed to assess the influence of surface temperature variations over diurnal, seasonal, and decadal timescales on heat transport in a layered porous media. The first analysis investigates the effect of variations in the decadal temperature gradient on the dimensionless temperature-depth profile. The second examines the impact of changing seasonal temperature amplitudes, while the final analysis explores the influence of diurnal amplitude fluctuations on subsurface thermal responses.

Fig. 5 illustrates the dimensionless subsurface temperature variation in a three-layered soil under four distinct decadal temperature rise scenarios, observed at four dimensionless time, i.e., $\bar{t} =$ 25, 50, 75, and 100. To explore the potential impact of climate change over a 100 year period, four distinct decadal temperature trends are considered, each reflecting a different magnitude of temperature rise. The dimensionless decadal temperature rise rate ($\bar{C}_0$) is varied from 0 to 0.0012, which corresponds to temperature increase from 0°C to 0.3°C per decade in real time. The Fig. 5 clearly indicates that the maximum temperature rise, resulting from increased

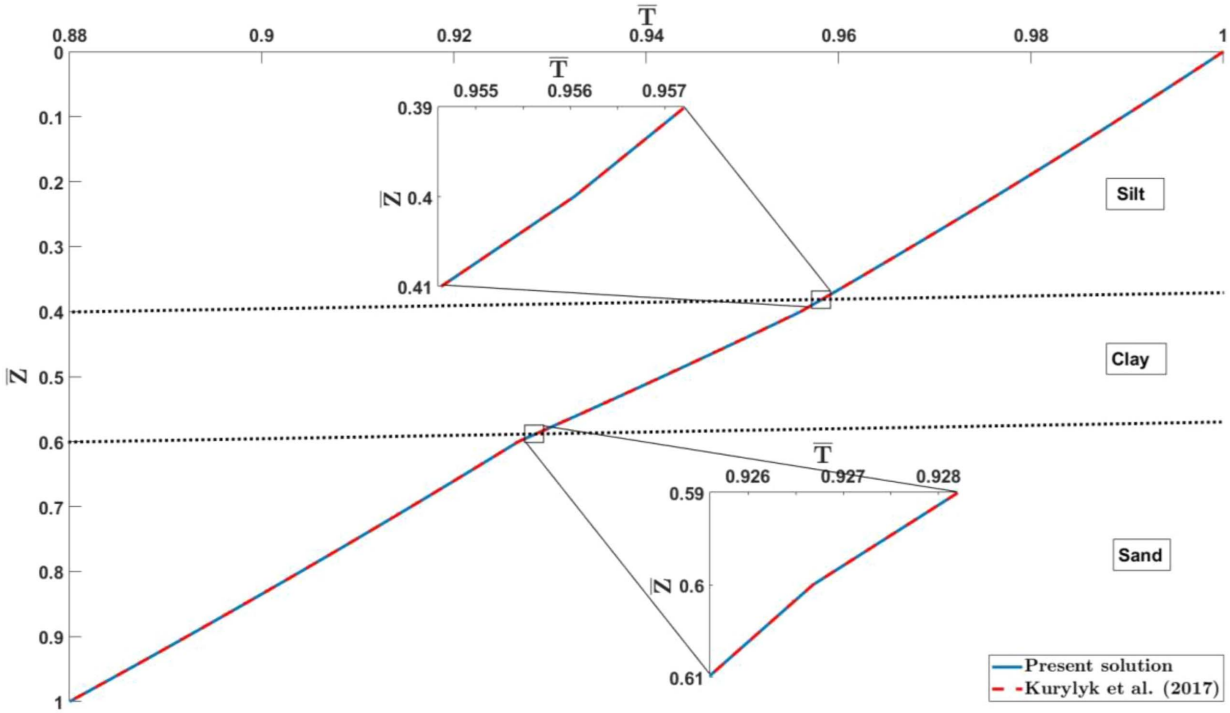

Fig. 3. Subsurface temperature-depth profiles predicted by the proposed solution and the solution by Kurylyk et al. (2017b) for a three-layered, steady-state flow system.

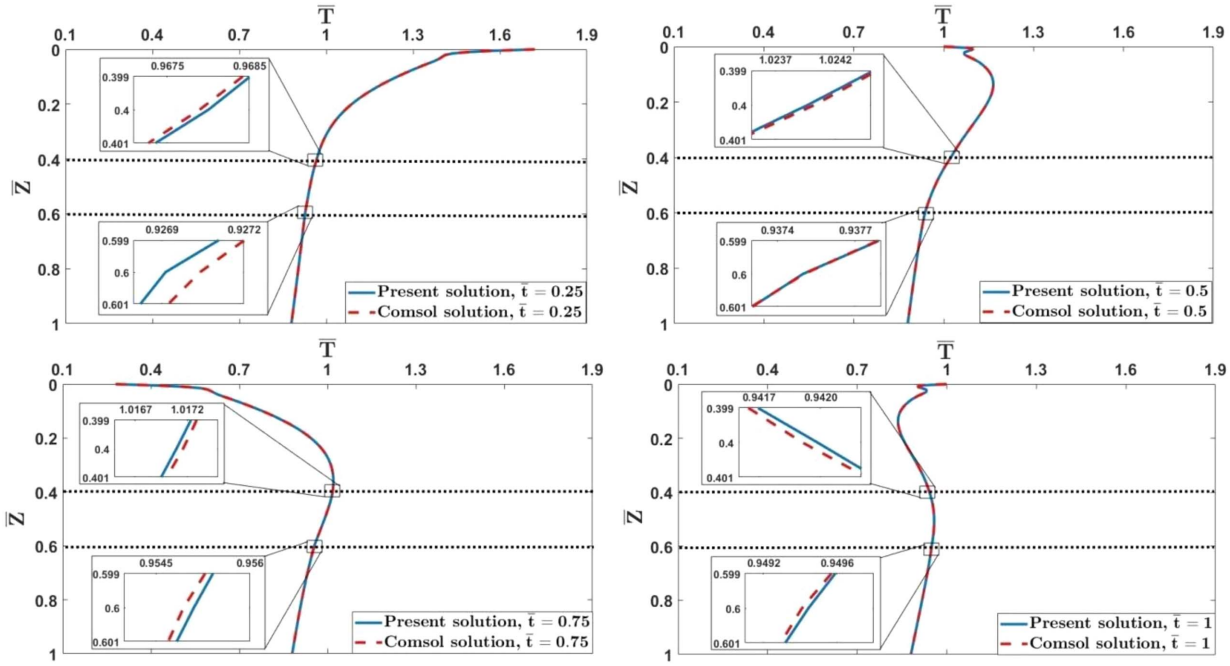

Fig. 4. Comparison of dimensionless subsurface temperature–depth profiles obtained from the proposed analytical solution and the COMSOL finite element model for a three-layered soil system subjected to a time-varying surface temperature boundary.

surface temperatures due to climate change, has the most significant impact at specific locations along the vertical direction. Three distinct locations within the flow domain, $z = 0.05$, 0.18, and 0.5, show a significant rise in soil temperature. These positions correspond to the peaks and valleys in the wavy temperature profile.

Fig. 6 shows the variation in the dimensionless temperature–depth profiles under different seasonal surface temperature amplitudes. To investigate the influence of seasonal atmospheric temperature fluctuations, four distinct dimensionless amplitudes ($\bar{A}_0$) ranging from 0 to 0.72 are considered. The temperature distributions are analyzed at four representative times throughout the year, corresponding to $\bar{t}$ ranging from 25 to 26. The analysis indicates that, in the absence of seasonal surface temperature fluctuations ($\bar{A}_0 = 0$), heat penetration into the subsurface is limited to the few meters of

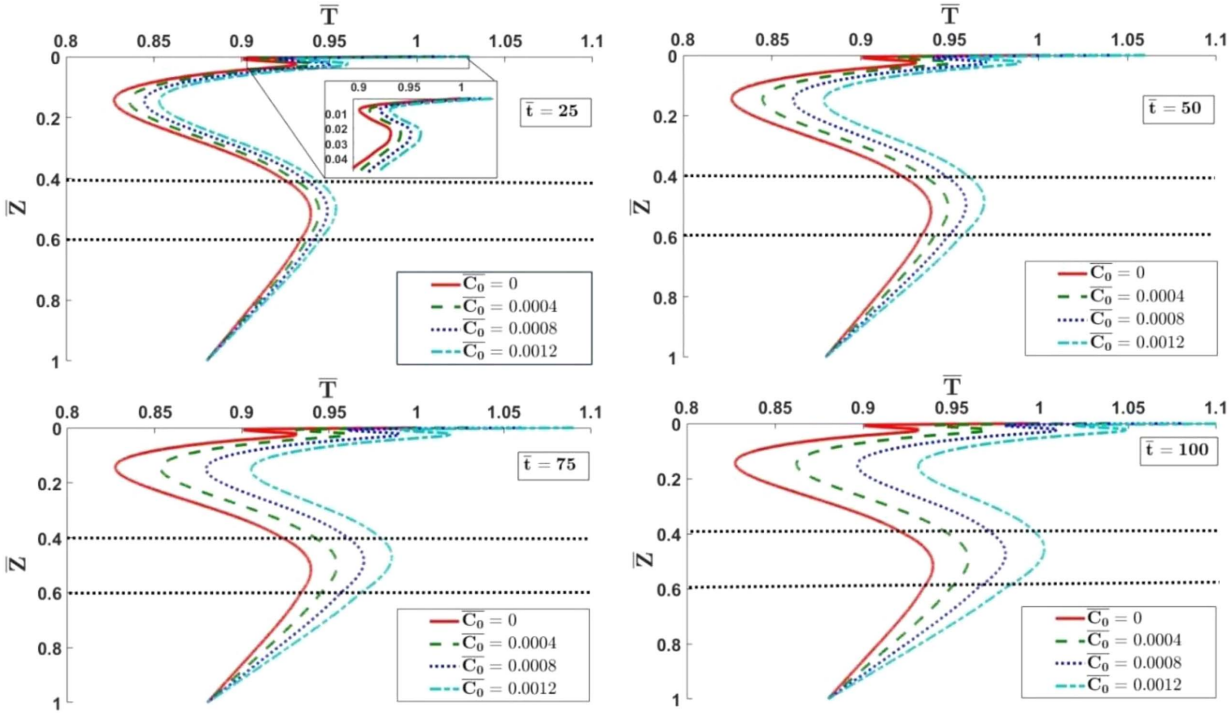

Fig. 5. Subsurface dimensionless temperature profiles corresponding to four different decadal surface temperature rise scenarios driven by climate change.

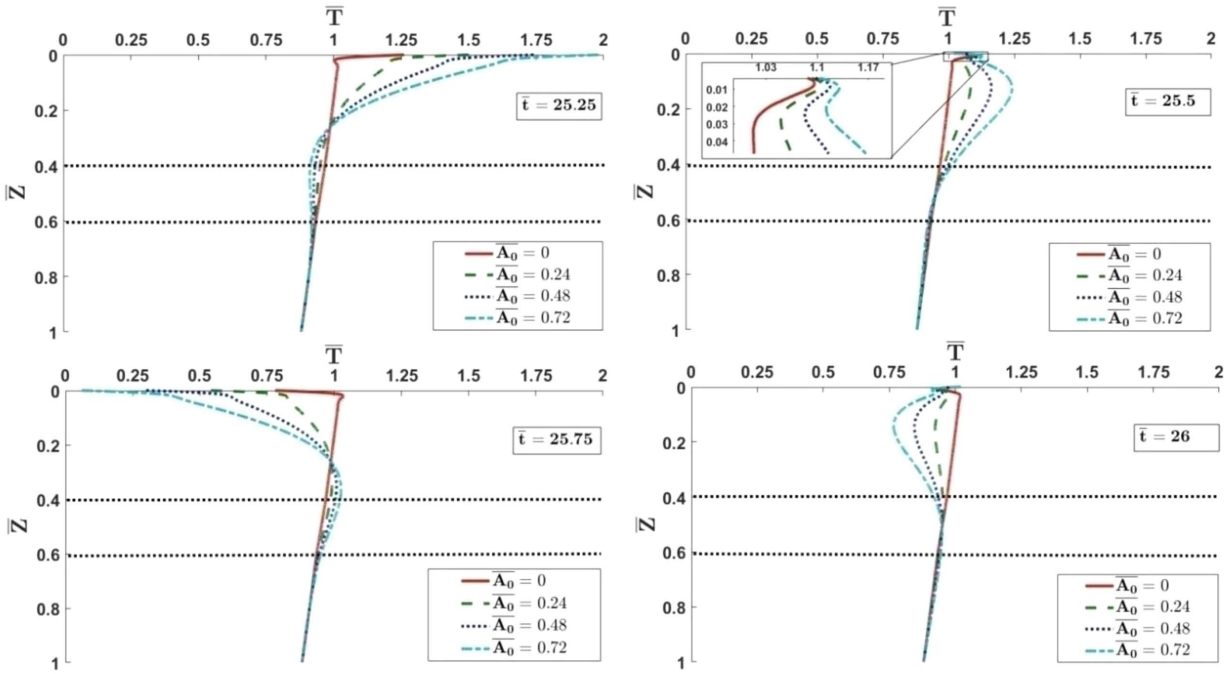

Fig. 6. Subsurface dimensionless temperature profiles corresponding to four different seasonal temperature amplitude rise scenarios.

depth. However, as the amplitude of seasonal temperature variation increases, the extent of temperature variability with depth also becomes more pronounced. The maximum depth of temperature penetration remains nearly constant across all other amplitudes of seasonal variation. Further, it is observed that, for all values of seasonal temperature variation amplitude, the temperature profiles consistently attain a unique dimensionless temperature value of one at a dimensionless depth, $\bar{z} = 0.25$, specifically at $\bar{t} = 25.25$ and 25.75.

The variation of dimensionless temperature with depth under diurnal surface temperature amplitudes is presented in Fig. 7. To assess the impact of daily temperature fluctuations, the analysis considers four distinct dimensionless diurnal temperature amplitudes ($\bar{B}_0$) ranging between 0 and 0.36. The temperature profiles are analyzed at four specific times throughout a complete day, corresponding to dimensionless times within a full cycle at dimensionless time 25. The figure clearly demonstrates that, on a daily time-scale, temperature

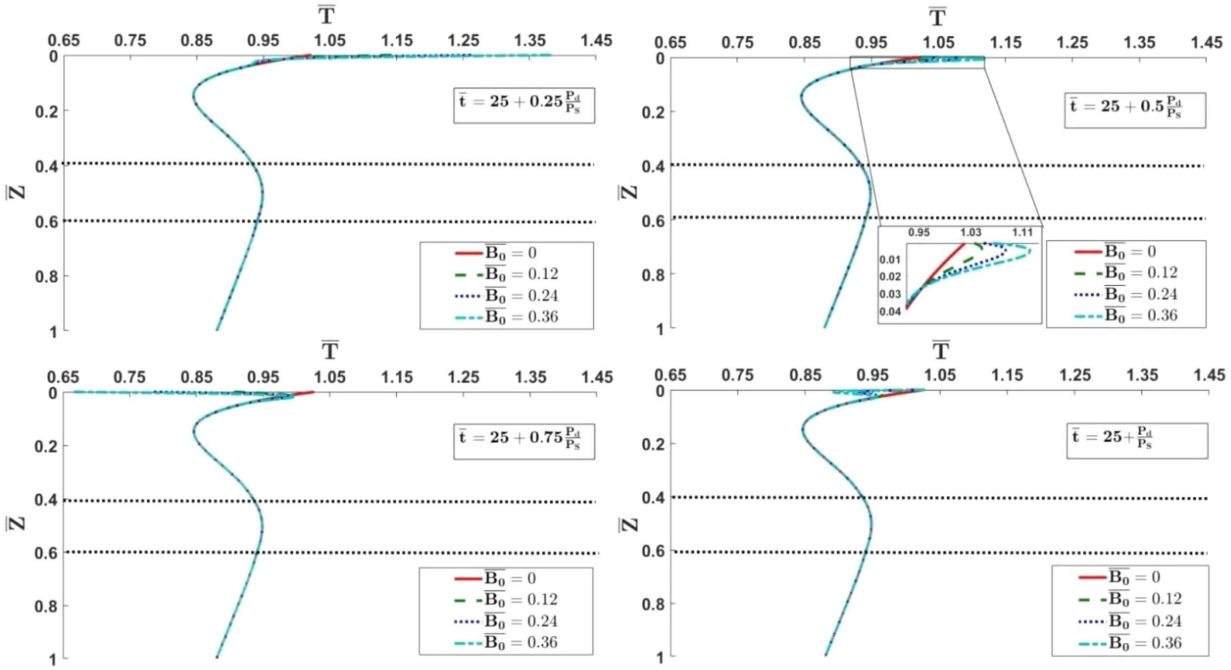

Fig. 7. Subsurface dimensionless temperature profiles corresponding to four different diurnal temperature amplitude rise scenarios.

variations are confined primarily to the upper half-meter of soil. This indicates that diurnal temperature changes have a minimal impact on the overall soil temperature distribution.

Fig. 8 illustrates the spatio-temporal variation of dimensionless temperature over a period of two dimensionless time units, corresponding to two years. The analysis demonstrates the progressive penetration of temperature into the soil profile driven by continuous seasonal and diurnal temperature fluctuations. The dotted curve represents the spatio-temporal contour corresponding to $\bar{T} = 1$. The analysis reveals that the temperature contours form inclined open loops in the depth–time plane, oriented at an acute angle to the vertical axis, reflecting the delayed and attenuated propagation of thermal waves with depth. The vertical propagation of these thermal waves is primarily attributed to seasonal surface temperature variations, while the influence of diurnal fluctuations is evident in the uppermost soil layer (up to a depth of $\bar{z} = 0.02$), as marked by horizontal kinks in the contour line near the surface. The lower portion of the contour plot reflects the influence of the constant temperature boundary condition at the base of the domain. Notably, a depression in the bottom contour surface is observed around dimensionless time 1, corresponding to the rise in surface temperature at time 0.25. Similarly, a bulge appears near time 1.55, associated with the surface temperature decline at time 0.75. These observations indicate an approximate delay of $\bar{t} = 0.8$ between surface temperature and corresponding thermal response near the bottom.

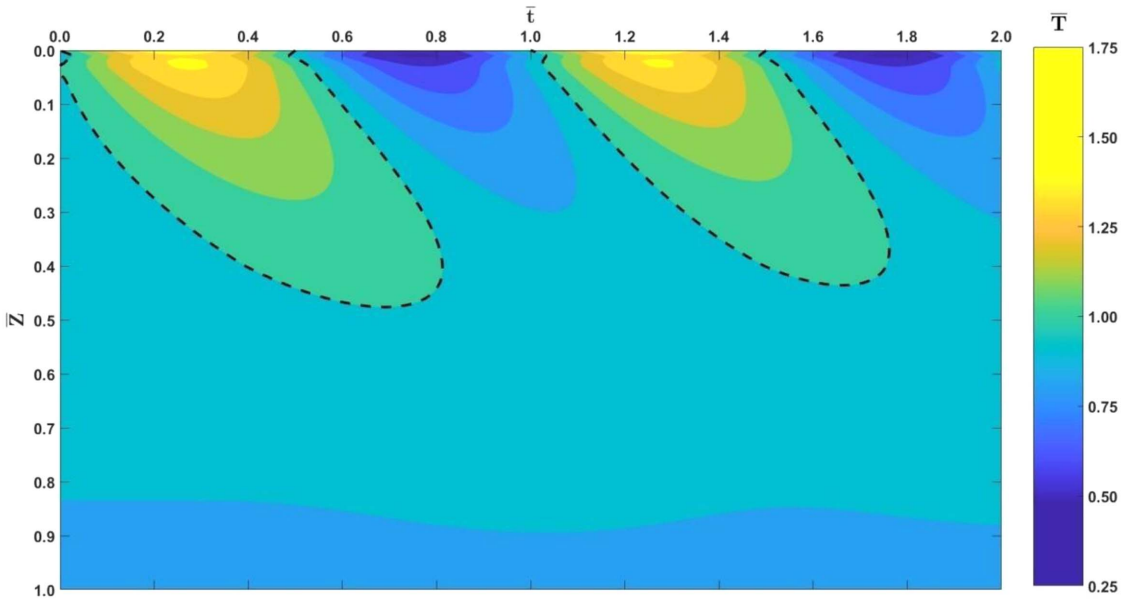

Fig. 8. Contour surface plots of subsurface dimensionless temperature profiles under a time-varying surface temperature boundary condition.

Impact of Soil Layering Orientation on Temperature Profile Variation

This study examines the variation of dimensionless temperature with depth across different soil layer configurations. Two distinct soil types, sand and clay, were selected due to their contrasting hydrogeological properties. The analysis was conducted using a stratified soil profile in which a layer with differing properties is sandwiched between two homogeneous layers. The thermal properties, layer positions, and boundary conditions used in the simulations are consistent with the values listed in Table 1. Two specific configurations were analyzed: 1) sand-clay-sand; and 2) clay–sand–clay, where the order of soil properties corresponds to the sequence of layers from the surface downward.

Fig. 9 presents the variation in dimensionless temperature-depth profiles for both soil configurations over a complete seasonal cycle, corresponding to dimensionless times ranging from 25 to 26. The analysis shows that, during the first half of the cycle (25 to 25.5), the sand–clay–sand configuration exhibits higher temperatures in the upper portion (up to a depth of $\bar{z} = 0.4$) of the flow domain compared to the clay–sand–clay configuration. This interval corresponds to the phase in which the surface temperature rises above the reference average, peaking at dimensionless time 25.25, and subsequently declines back to the reference level by 25.5. The observed temperature difference is attributed to the higher thermal conductivity of the top layer in the sand–clay–sand configuration, which facilitates greater heat penetration and results in elevated temperatures near the surface during this warming phase.

In contrast, the trend reverses in the latter half of the cycle (25.5 to 26). Between 25.5 and 25.75, the surface temperature drops below the reference average, reaching its seasonal minimum at dimensionless time 25.75. During this cooling phase and the subsequent interval (25.75 to 26), the sand–clay–sand configuration exhibits higher temperatures in the upper soil layer (up to a depth of $\bar{z} = 0.4$) than the sand–clay–sand configuration. This reversal is attributed to the lower thermal conductivity and higher volumetric heat capacity of the clay top layer, which limits heat loss and enhances thermal retention near the surface. It is also noteworthy that, across all four temporal snapshots, temperature variations in the deeper layers remain negligible in both configurations.

Performance Comparison between the Proposed Analytical Model and the Deng et al. (2014) Model

The methodology used to develop the proposed analytical model is a modified version of the approach originally introduced by Deng et al. (2014). While their solution technique was initially formulated for 1D contaminant transport in layered media, the governing differential equations for contaminant transport and advection-diffusion-based heat transfer in porous media share a similar mathematical structure. Leveraging this similarity, the present study adopts and extends their methodology, introducing key modifications to enhance its broader applicability in stratified subsurface environments.

A major advancement introduced by Deng et al. (2014) was the intrinsic incorporation of heterogeneity due to the layered nature of porous media directly into the transient analytical formulation. Traditional steady-state models typically address such heterogeneity by solving the governing equations independently for each layer while enforcing continuity of the state variable and flux at the interfaces (Kurylyk et al. 2017b; Sarmah and Barua 2015). Although such techniques can be extended to transient systems, they often require solving nonlinear transcendental equations to determine eigenvalues, which increases mathematical complexity with additional layers (Liu and Si 2008; Sarmah et al. 2022). In contrast, Deng et al. (2014) integrated spatial variability of flow parameters within a unified solution framework, eliminating the need for explicit domain partitioning and interface matching. This significantly simplifies the analytical treatment of stratified systems while ensuring continuity of state variables and fluxes across interfaces.

Deng et al. (2014) decomposed the state variable (in their case, contaminant concentration) into two components. The first component captures the transient flow behavior throughout the domain while inherently accounting for the layered structure considering

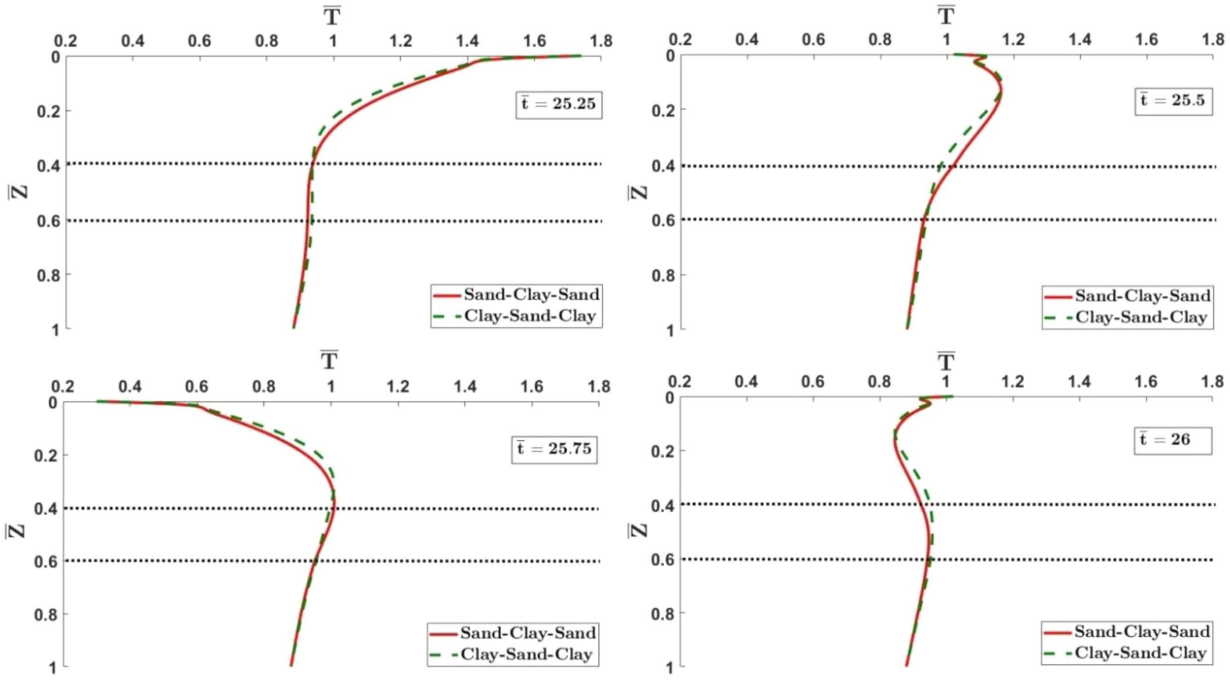

Fig. 9. Subsurface dimensionless temperature profiles for four different seasonal temperature amplitude scenarios across various soil layer order configurations.

homogeneous boundary; this represents the novel aspect of their approach. The second component is a second-degree spatial polynomial with time-dependent coefficients, designed to represent the influence of transient boundary conditions [refer to Eq. (17) in Deng et al. (2014)]. In the present study, we modify the second component of Deng et al. (2014)'s formulation by replacing the polynomial representation with a steady-state solution of the governing equation considering transient boundary condition. The first component of the solution, as developed by Deng et al. (2014), is unchanged.

The primary motivation for modifying the solution methodology proposed by Deng et al. (2014) is to improve its applicability to a broader range of conditions, particularly near steady-state scenarios, and to enable its extension to higher spatial dimensions (2D and 3D). Since the utility of analytical techniques is inherently linked to the type of governing equation they address, refining the solution framework is essential to ensure its relevance in diverse scenarios. Such modifications aim to extend the solution's applicability to fields, including contaminant transport, heat flow in aquifers, and diffusive transport in layered media.

To facilitate the comparative analysis between the models, we consider a three-layer soil profile arranged in a sand–clay–sand configuration (from top to bottom), with enhanced hydrothermal properties to accentuate the differences between the two models. The thermal conductivities of sand and clay are set to 4.01 and 0.98 W/m/°C, respectively, while their corresponding volumetric heat capacities are taken as 1.95×10^6 and 3.564×10^6 J/m^3/°C. It is important to note that these parameter values lie within the range typically observed in field conditions (Baek et al. 2022; Gabrielsson et al. 1997). All other parameters remain consistent with those listed in Table 1.

To perform this analysis, the top boundary surface temperature is prescribed as a constant nondimensional value of 1, since flow systems subjected to temporally varying boundary conditions do not attain a steady-state regime. The simulation is conducted over an extended period until temporal variations in the temperature within the flow domain become negligible, indicating convergence to a steady-state condition. Fig. 10 illustrates the steady-state distributions of dimensionless temperature and dimensionless temperature flux predicted by the proposed model, compared against the corresponding results from the model developed by Deng et al. (2014). The dimensionless temperature flux is calculated using the relation $\bar{J}_T = -\omega_i(\partial\bar{T}/\partial\bar{z}) + \bar{T}$, derived from Eq. (9).

As evident from the figure, the steady-state dimensionless temperature profiles produced by the proposed model closely aligns with that of Deng et al. (2014) throughout the domain, with noticeable deviations occurring primarily at the interfaces between soil layers. The proposed solution exhibits distinct kinks at these interfaces, attributed to abrupt changes in thermal properties. In contrast, the model by Deng et al. (2014) fails to capture these sharp transitions, as it employs polynomial expressions in the solution to capture the effects of nonhomogeneous boundaries, whereas the present model utilizes the exact steady-state solution, enabling a more accurate representation of interface behavior. In addition to the temperature profiles, the corresponding dimensionless heat flux distributions from both models are also presented. For a steady-state system, the heat flux should remain constant throughout the domain, a condition accurately captured by the proposed model. However, the heat flux derived from the Deng et al. (2014) model remains consistent across the layers but shows discontinuities at the interfaces. To address this shortcoming, we have modified the Deng et al. (2014) model by replacing the polynomial formulation with the exact steady-state solution, thereby improving its ability to handle layered media with discontinuous thermal properties at near steady-state condition. Further comparative analysis under transient flow conditions indicates that both models produce closely matching results in terms of temperature distribution and heat flux. However, neither model accurately captures the localized heat flux variations at the interfaces under transient conditions.

Extending the Deng et al. (2014) model to higher spatial dimensions (2D and 3D) is likely to introduce significant ambiguity, as the solution framework relies on second-order polynomial expressions whose coefficients depend on the specific boundary conditions imposed on the domain. When generalizing the model to higher dimensions, the polynomial form must also be reformulated accordingly, leading to increased complexity. As the spatial dimensionality

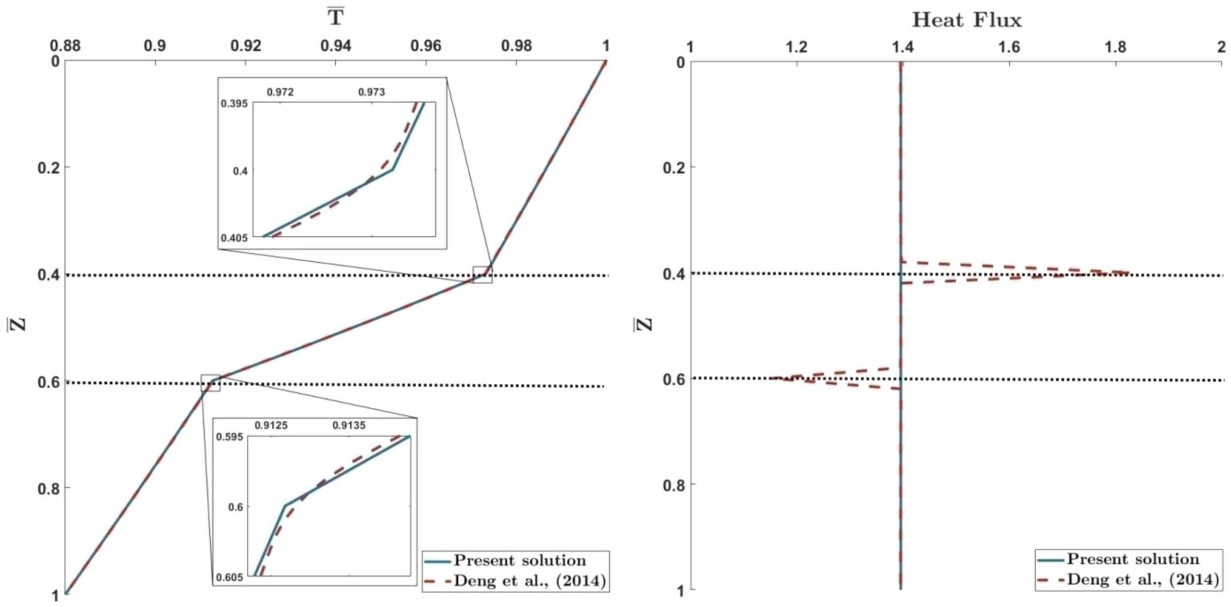

Fig. 10. Comparison of steady-state dimensionless temperature and heat flux profiles obtained from the proposed solution and the model by Deng et al. (2014).

J. Hydrol. Eng., 2026, 31(2): 04025060

increases, the number of boundary surfaces grows, making it increasingly difficult to incorporate all boundary conditions consistently. As a result, determining the appropriate form of higher-order polynomials, and selecting the suitable combinations of spatial variables, may lead to ambiguity in formulation and implementation.

In contrast, the modified approach proposed in this study offers a more robust and adaptable framework for addressing problems in higher spatial dimensions. Since steady-state solutions for layered aquifer systems are readily available in the literature (Haji-Sheikh et al. 2003; Sarmah and Barua 2015), the methodology adopted here can be extended to higher-dimensional problems by replacing the polynomial-based representations in the analytical solution with these well-established steady-state counterparts.

Sensitivity Analysis of Dimensionless Temperature Distribution

Fig. 11 presents the sensitivity variation of the dimensionless temperature-depth profile $(\bar{T})$ to variations in key geothermal properties, notably, the dimensionless thermal conductivity (ω_i) and dimensionless volumetric heat capacity (σ_i). The definitions of these dimensionless parameters are provided in Eq. (8). The analysis reveals that a slight increase in the dimensionless thermal conductivity (ω_1) of the first layer induces a negative sensitivity in the temperature profile within the first and second soil layers during the first half of the year, particularly near the interface between these layers around the dimensionless time $\bar{t} = 0.25$. In contrast, during the second half of the year, the temperature $(\bar{t})$ exhibits positive sensitivity to ω_1 in the upper two layers, with the peak response observed near $\bar{t} = 0.75$, again close to the layer interface. It is important to note that $\bar{t} = 0.25$ and 0.75 correspond to the seasonal maximum and minimum boundary temperatures, respectively. In the third layer, the $\bar{T}$ is found insensitive to ω_1.

The dimensionless temperature $\bar{T}$ exhibits positive sensitivity to the dimensionless volumetric heat capacity (σ_1) in the shallow region of the first layer, primarily during the first half of the season, with the effect most pronounced up to a depth of $\bar{z} = 0.3$ and peaking around $\bar{t} = 0.25$. In contrast, during the second half of the season, a negative sensitivity is observed, predominantly within the uppermost $\bar{z} = 0.1$ depth, with the peak occurring near $\bar{t} = 0.7$. In addition, $\bar{T}$ is found to be largely insensitive to the dimensionless thermal conductivity (ω_2) of the second layer and dimensionless volumetric heat capacity (σ_3) of the third layer across the entire soil profile and throughout all seasons.

The dimensionless volumetric heat capacity (σ_2) of the second layer induces a slight positive sensitivity in the middle layer of the soil profile around $\bar{t} = 0.5$, primarily within the depth range of $\bar{z} =$ 0.4 to 0.45. Outside this narrow depth–time window, the temperature response is largely insensitive to variations in σ_2. Further, the dimensionless thermal conductivity (ω_3) of the third layer exhibits positive sensitivity to $\bar{T}$ within the second and third layers during the early phase of the simulation, approximately between $\bar{t} = 0$ to 0.3, with peak sensitivity occurring near the interface between the second and third layers. Beyond this initial period, the temperature becomes largely insensitive to this parameter across the entire domain and remains insensitive within the first layer throughout the year.

Inverse Estimation of Groundwater Flux

Numerous heat transfer models have been developed and widely applied in field investigations to estimate vertical groundwater flux, along with the thermal and hydraulic properties of subsurface sediments (Kampen et al. 2022; Klepikova et al. 2016; Lin et al. 2022; Liu et al. 2024; Simon and Bour 2023). These models commonly rely on inverse modeling techniques to infer key geothermal parameters from observed temperature data. Although substantial advancements have been made in quantifying vertical fluxes and associated properties, to the best of our knowledge, no previous study has specifically addressed the estimation of vertical water flux in a layered subsurface media using time-series temperature-depth profile data. In this study, a tailored analytical model is integrated within an inverse modeling framework to enable robust parameter estimation based on the propagation of thermal signals through the subsurface, thereby improving the method's practicality and applicability in real-world field settings.

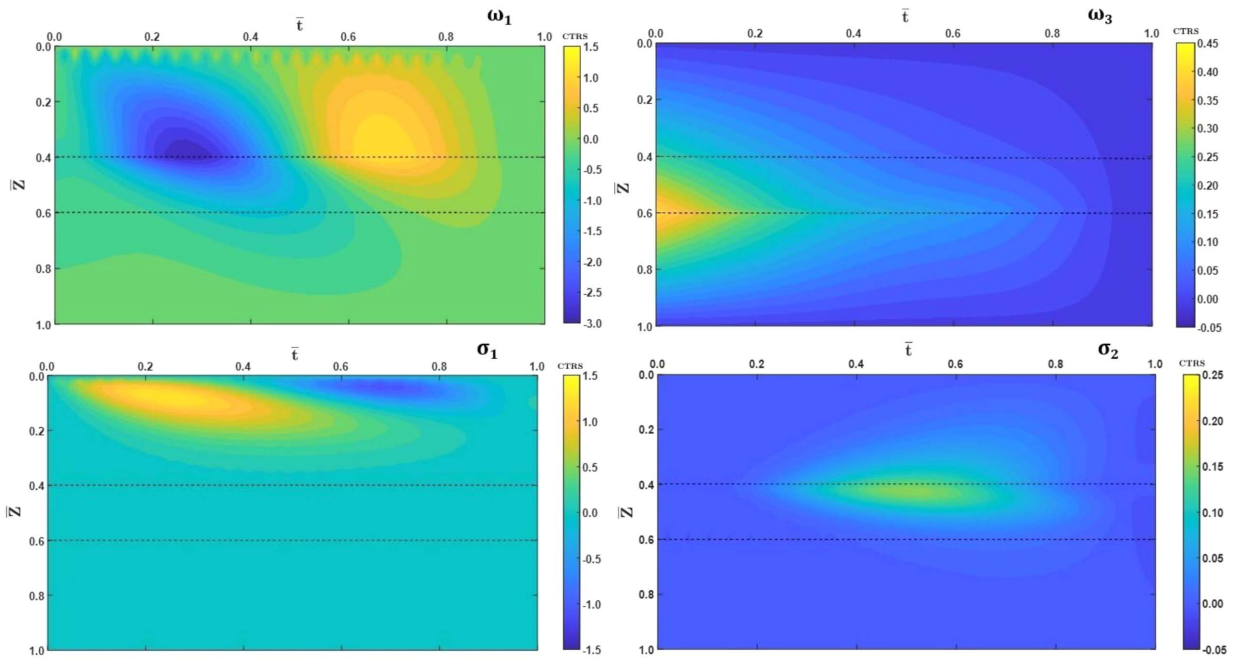

Fig. 11. Contour representation of the central total relative sensitivity index pertaining to dimensionless depth–temperature profile in response to geothermal parameters.

To perform the inverse parameter estimation, the forward model (analytical solution) is run with known (true) parameter values as listed in Table 1. In this study, the true value for vertical groundwater flux (q) is taken as 0.33 m/year. Based on these inputs, the model simulates a synthetic temperature-depth profile, from which observation data are extracted. Specifically, temperature values are recorded at five equally spaced spatial locations within the top 10 m of the soil column, at six distinct time intervals over a six-month period.

To emulate the uncertainties inherent in real field measurements, Gaussian white noise with zero mean and variance of σ^2 is superimposed on the simulated temperature data. This yields a synthetic data set defined as $T_i^{\text{syn}} = T_i^{\text{Forward}} + N(0, \sigma^2)$, where $N(0, \sigma^2)$ represents normally distributed random noise with zero mean and σ^2 variance, and i represents different data points. A total of 30 synthetic data points are used in the inverse analysis, five spatial points for each of the six time-steps. The standard deviation (σ) of the added noise is set to 5% of the standard deviation of the forward model output generated using the true parameter values.

The inverse modeling process aims to estimate the parameter q by minimizing the normalized sum of squared relative errors between the synthetic data and the corresponding model predictions. The objective function for this minimization problem can be written as

$$\min\ \phi(q) = \sum_{i=1}^{30} \left[\frac{T_i^{\text{syn}} - T_i^{\text{model}}(q)}{T_i^{\text{syn}}} \right]^2 \tag{47}$$

$$\text{subjected to } q > 0 \tag{48}$$

This optimization is carried out using a genetic algorithm (GA) via MATLAB's built-in optimization toolbox. The GA is a powerful global optimization technique inspired by the principles of natural selection and evolutionary biology. It begins by generating an initial population of candidate solutions (chromosomes) within predefined bounds. Each chromosome is evaluated using a fitness function, and the most suitable candidates are selected for genetic operations such as crossover and mutation. This iterative evolutionary process continues until the algorithm converges to a globally optimal solution. The GA is particularly well-suited for solving complex, nonlinear, and nondifferentiable optimization problems, situations where conventional gradient-based methods often perform poorly or become trapped in local optima. The GA parameters employed in the optimization are summarized in Table 2.

The results presented in Table 3 demonstrates that utilizing a total of 30 data points, collected from the top 10 m of the soil profile over a six-month period, enables accurate estimation of vertical groundwater flux (q). Remarkably, these parameters are predicted with a root mean square error (RMSE) of 0.121°C, even after incorporating uncertainties in the synthetic data set. This highlights the robustness and reliability of the proposed inverse modeling approach for accurately estimating the vertical groundwater flux. Further, the study underscores the necessity of accounting for subsurface layering in natural aquifers. In the absence of a layered solution, there is a common tendency to adopt models assuming homogeneous properties throughout the profile. To evaluate the implications of this simplification, an additional analysis was conducted, wherein the aquifer was assumed to be homogeneous with the properties of the topmost layer. Table 3 presents a comparison of the true and estimated values of vertical groundwater flux under these two conceptualizations. When the stratified (three-layer) model was used, the inverse estimation yielded a recharge value of 0.342 m/yr, closely matching the true value. In contrast, assuming a homogeneous aquifer resulted in a significantly overestimated flux of 0.48 m/yr, underscoring the potential errors introduced by neglecting vertical heterogeneity.

Table 2. Parameter settings of the genetic algorithm used for the optimization

Parameter	Value
Population size	100
Number of generations	100
Crossover probability	60%
Mutation probability	2%–5%

Table 3. Comparison of inverse estimates of vertical groundwater flux for layered and homogeneous aquifer configurations

Soil type	True value (m/yr)	Estimated value (m/yr)	RMSE (°C)
Three-layer (silt–clay–sand)	0.33	0.342	0.121
Singe-layer (silt)	0.33	0.48	0.156

Field Application

The developed model was applied to estimate streambed flux using field-observed temperature data reported by Kurylyk et al. (2017a). The details of the methodology and problem conceptualization are presented in the section "Field Data Interpretation." The thermal conductivities of the organic mud layer (upper layer) and sand were taken as 1.35 and 2.74 W/m/°C, respectively, with corresponding volumetric heat capacities of 2.934×10^6 and 2.96×10^6 J/m^3/°C (Kurylyk et al. 2017b). The thickness of the upper layer (d_1) was 0.1518 m (corresponding dimensionless depth $\bar{d}_1 = 0.333$), while the total depth of the domain (d) was 0.4554 m.

The initial condition for the heat transport problem was fitted using a straight-line representation for each layer, as described in Eq. (44). The resulting fitting coefficients were $c_1 = 0.5652$, $c_2 = -0.3492$, $c_3 = 0.4828$, and $c_4 = -0.0732$, with an R^2 value of 0.9946. Similarly, the upper boundary condition was expressed using a Fourier series [Eq. (42)], achieving an R^2 value of 0.9980. A comparison of the observed and fitted initial and boundary conditions, as shown in Fig. 12, demonstrates strong agreement, confirming that the assumed conditions adequately represent the observed data.

To estimate vertical water flux through the streambed, an inverse modeling approach (detailed in the section "Inverse Estimation of Groundwater Flux") was employed using the objective function defined in Eq. (47), in combination with a GA implemented through MATLAB's built-in optimization toolbox. The GA parameters utilized in the optimization are summarized in Table 2. A total of 20 data points were considered, corresponding to dimensionless depths of 0.1515, 0.2424, 0.5758, and 0.9394, and dimensionless times of 0.000547, 0.0011, 0.0016, 0.0022, and 0.0027. These values corresponded to dimensional depths of 0.0690, 0.1104, 0.2622, and 0.4278 m and dimensional times of 0.2, 0.4, 0.6, 0.8, and 0.98 days, respectively. The flux search domain was set to $-100 < q < 100$ m/yr, since the direction of flow (upward or downward) was initially unknown.

Minimization of the objective function [Eq. (47)] yielded an estimated flux of –56.0207 m/yr with a minimum RMSE of 0.0586°C, indicating upwelling conditions. For comparison, Kurylyk et al. (2017b) reported a flux of –68 m/yr based on a steady-state heat transport model. The discrepancy arises because Kurylyk et al. (2017b) fitted their steady-state model to temporally averaged temperature values at each depth, whereas the present model accounts

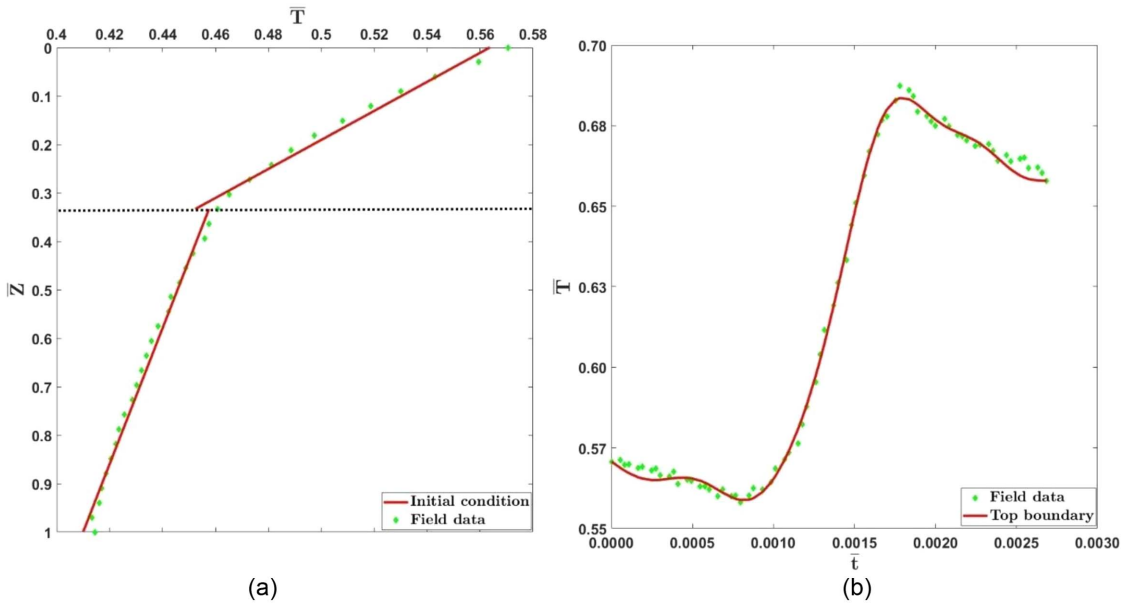

Fig. 12. Comparison of observed and modeled data sets in dimensionless form for (a) the initial condition; and (b) the top boundary condition.

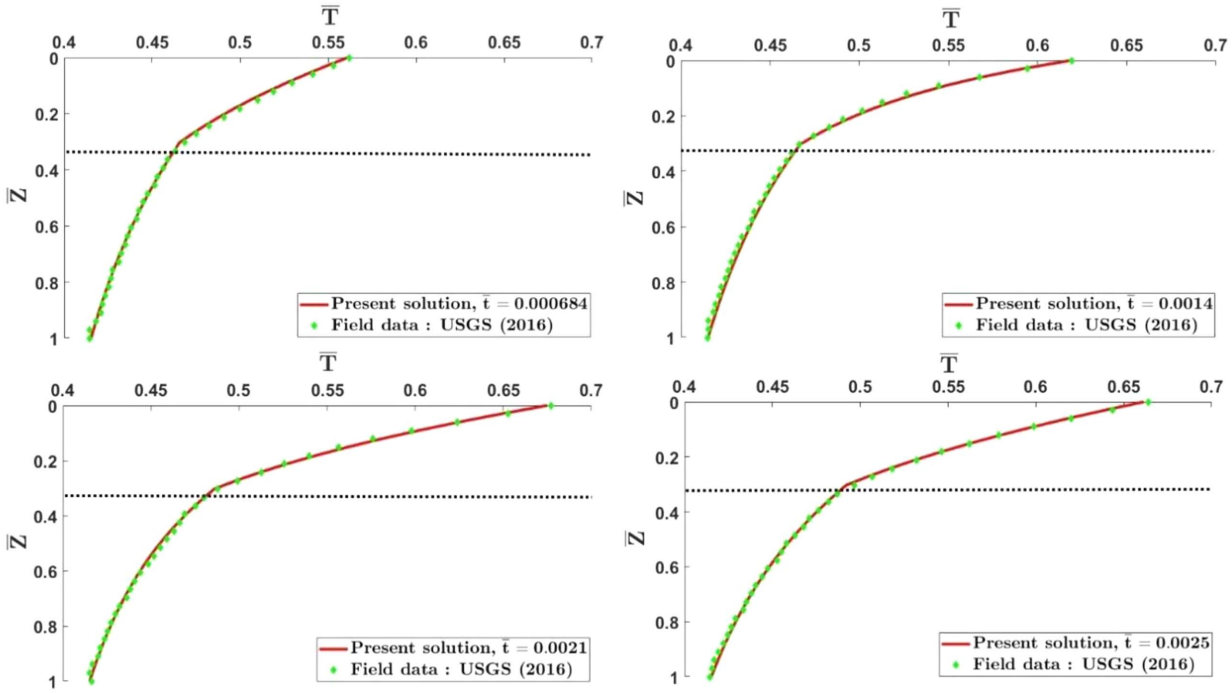

Fig. 13. Dimensionless temperature–depth profiles at different times for field data and the present solution using the estimated flux.

for the full transient variation of the observed data. This enables a more realistic representation of the system.

The inversely estimated flux was subsequently applied as a known input to predict complete temperature-depth profiles at four different times, as presented in Fig. 13. The simulated results showed close agreement with observed field data across the entire domain, demonstrating the robustness and reliability of the estimated flux.

Limitations and Future Scope

Despite the robustness and flexibility of the analytical framework developed in this study for simulating transient heat transfer in stratified subsurface media, several limitations warrant consideration. The model is formulated in one dimension, assuming vertical heat transport only, thereby neglecting lateral heat fluxes that may become significant in environments with pronounced horizontal temperature gradients or anisotropic thermal conductivities. It also assumes a uniform vertical water flux, whereas natural systems often exhibit spatially and temporally variable fluxes due to processes such as infiltration, evapotranspiration, and water table fluctuations. In addition, each soil layer is treated as internally homogeneous, overlooking intralayer heterogeneities that can influence heat transport dynamics. Last, the current model does not account for nonlinear processes such as phase change (e.g., freezing and thawing), temperature-dependent thermal properties, or moisture variations,

all of which may be critical in certain hydrogeological or climatic scenarios.

Future research could address some of these limitations by incorporating temporally varying top boundary fluxes in conjunction with soil–water characteristic curves. Such enhancement would enable more realistic analyses of transient moisture pulses generated by intense rainfall. Moreover, explicitly accounting for the dependence of thermal properties on soil moisture content would improve the accuracy of temperature profile predictions and vertical flux estimations.

Conclusion

This study presents a comprehensive analytical framework for simulating transient heat transport and performing inverse estimation of groundwater flux in a stratified medium. The proposed model incorporates realistic surface temperature variations and accounts for soil heterogeneity through a scalable, analytical solution. Model performance is validated through detailed comparisons with existing analytical approaches and COMSOL-based numerical simulations, demonstrating strong agreement and reinforcing the reliability of the formulation. A local sensitivity analysis, numerical validation, and inverse modeling with observed field data demonstrate the robustness, accuracy, and practical applicability of the method. Based on the analysis and findings, the following key conclusions can be drawn:

- The model effectively captures the impact of diurnal, seasonal, and decadal surface temperature variations on subsurface heat transport. Among these, seasonal variations have the most significant influence on temperature penetration depth, while diurnal effects remain confined to the top 0.5 m of the soil.
- Temperature contour plots exhibit inclined open-loop structures in the depth–time plane, indicating delayed and dampened thermal wave propagation with depth. An approximate lag of 0.8 dimensionless time units was observed between surface temperature changes and subsurface thermal responses near the water table.
- Sensitivity analysis shows that the dimensionless temperature distribution is most strongly affected by the thermal conductivity and volumetric heat capacity of the top soil layer, particularly near layer interfaces and during seasonal temperature extremes, while deeper layers have minimal sensitivity to their geothermal properties.
- The model successfully estimated vertical flux from field data, achieving high accuracy (RMSE ≈ 0.0586°C) using observed transient temperature profiles of a layered streambed.

Appendix I. Derivation of the Quasi-steady-state Component ($\bar{T}_{st}$) of the Analytical Model

The dimensionless governing equation for quasi-steady-state heat transfer in a subsurface media, as referenced in the main text [Eq. (16)], is expressed as

$$\frac{\partial}{\partial \bar{z}}\left(\omega_i \frac{\partial \bar{T}_{st}}{\partial \bar{z}}\right) - \frac{\partial \bar{T}_{st}}{\partial \bar{z}} = 0 \quad (\bar{d}_{i-1} \le \bar{z} \le \bar{d}_i) \tag{49}$$

Solving the equation for a given soil layer (ith layer) yields (Piskunov 1974)

$$\bar{T}_{sti} = P_i + Q_i \exp\left(\frac{\bar{z}}{\omega_i}\right) \tag{50}$$

where ω_i is considered a constant within a given layer, as it remains uniform, but it varies when transitioning to a different layer. In an N-layer soil system, Eq. (50) generates $2N$ unknown coefficients. However, there are an equal number of known boundary conditions: one at the top surface [Eq. (19)]; another at the bottom [Eq. (20)]; and the remaining conditions ensuring temperature continuity [Eq. (17)] and heat flux continuity [Eq. (18)] at $(N-1)$ interface points between the soil layers. By applying the relevant boundary and interface conditions to Eq. (50), the coefficients (P_i and Q_i) pertaining to the quasisteady-state solution for the dimensionless temperature in an N-layer soil system is obtained as

$$P_i = \frac{\bar{T}_T(t)\exp(\alpha) - \bar{T}_B}{\exp(\alpha) - 1}, \quad (1 \le i \le N) \tag{51}$$

$$Q_i = Q_{i-1}\exp\left[\bar{d}_{i-1}\left(\frac{1}{\omega_{i-1}} - \frac{1}{\omega_i}\right)\right], \quad (2 \le i \le N) \tag{52}$$

where

$$Q_1 = \frac{\bar{T}_B - \bar{T}_T(t)}{\exp(\alpha) - 1} \tag{53}$$

and

$$\alpha = \sum_{i=1}^{N-1}\left[\bar{d}_i\left(\frac{1}{\omega_i} - \frac{1}{\omega_{i+1}}\right) + \left(\frac{\bar{d}}{\omega_{i+1}}\right)\right] \tag{54}$$

It is important to note that, even if $\bar{T}_{st}$ includes the time-dependent variable $\bar{T}_T(t)$, the proposed solution [Eq. (50)] still satisfies the governing equation [Eq. (49)].

Appendix II. Derivation of the Transient Component ($\bar{U}$) of the Analytical Model

The analytical expression for $\bar{U}(\bar{z}, \bar{t})$ is obtained by solving Eq. (33) along with the initial and boundary conditions [Eqs. (28)–(30)] using the GITT (Liu et al. 2000; Mikhailov and Ozisik 1984). To solve this boundary value problem, an integral transform pair is formulated. This pair is constructed by selecting appropriate eigenfunctions corresponding to the auxiliary Sturm–Liouville boundary value problem

$$\frac{d^2\psi_m(\bar{z})}{d\bar{z}^2} + (N_m)^2\psi_m(\bar{z}) = 0, \quad m = 1, 2, 3 \tag{55}$$

where ψ_m = the eigenfunctions of the auxiliary problems defined in Eq. (55). This equation is solved under homogeneous boundary conditions, $\psi_m(\bar{z})|_{\bar{z}=0,\bar{d}} = 0$. The solution to the Sturm–Liouville problem [Eq. (55)] with these specified boundary conditions is given by

$$\psi_m(\bar{z}) = \sin(N_m\bar{z}), \qquad N_m = \frac{m\pi}{\bar{d}} \tag{56}$$

According to the definition of the eigenfunctions in the Sturm–Liouville boundary value problem, $\psi_m(\bar{z})$ satisfies the orthonormal properties (Haberman 2013), expressed as

$$\frac{1}{(\beta_m)^{1/2}(\beta_r)^{1/2}}\int_0^{\bar{d}} \psi_m(\bar{z})\psi_r(\bar{z})d\bar{z} = \delta_{mr} \tag{57}$$

where δ_{mr} = a Kronecker delta function whose value is 1 for $m = r$, and $\delta_{mr} = 0$ for $m \neq r$; and

$$\beta_m = \int_0^{\bar{d}} \sin^2(N_m \bar{z}) d\bar{z} \tag{58}$$

Here, it is important to note that r serves as a dummy index for m. Utilizing the orthogonality property of the eigenfunction $\psi_m(\bar{z})$, the forward transform is formulated as follows:

$$\tau_m(\bar{t}) = \frac{1}{(\beta_m)^{1/2}} \int_0^{\bar{d}} \bar{U}(\bar{z}, \bar{t}) \psi_m(\bar{z}) d\bar{z} \tag{59}$$

and the corresponding inverse transform is given by

$$\bar{U}(\bar{z}, \bar{t}) = \sum_{m=1}^{M \to \infty} \tau_m(\bar{t}) \frac{\psi_m(\bar{z})}{(\beta_m)^{1/2}} \tag{60}$$

For computation ease, the upper limit of the summation term is truncated to a finite value M, selected to be sufficiently large to achieve the desired accuracy.

Applying the integral operator $(1/(\beta_m)^{1/2}) \int_0^{\bar{d}} (\cdot) \psi_m(\bar{z}) d\bar{z}$ to Eq. (33) with minor adjustments for evaluating the unknown transient function $\tau_m(\bar{t})$ yields

$$\begin{aligned} &\frac{1}{(\beta_m)^{1/2}} \int_0^{\bar{d}} \sigma(\bar{z}) \frac{\partial \bar{U}}{\partial \bar{t}} \psi_m(\bar{z}) d\bar{z} \\ &\quad + \frac{1}{(\beta_m)^{1/2}} \int_0^{\bar{d}} \left\{ -\frac{\partial}{\partial \bar{z}} \left[\omega(\bar{z}) \frac{\partial \bar{U}}{\partial \bar{z}} \right] + \frac{\partial \bar{U}}{\partial \bar{z}} \right\} \psi_m(\bar{z}) d\bar{z} \\ &= -\frac{1}{(\beta_m)^{1/2}} \int_0^{\bar{d}} \sigma(\bar{z}) \frac{\partial \bar{T}_{st}}{\partial \bar{t}} \psi_m(\bar{z}) d\bar{z} \end{aligned} \tag{61}$$

By substituting the expression for $\bar{U}(\bar{z}, \bar{t})$ from Eq. (60) into the equation, replacing the index m with a dummy index r, and rearranging the integrals, we obtain a system of simultaneous ordinary differential equations

$$\sum_{r=1}^{M} D_{mr} \frac{d\tau_r(\bar{t})}{d\bar{t}} + \sum_{q=1}^{M} E_{mr} \tau_r(\bar{t}) = F_m(\bar{t}) \tag{62}$$

The following section outlines the intermediate steps involved in deriving Eq. (62) from Eq. (61). The first term of Eq. (62) corresponds to first term of Eq. (61) and similarly for the other terms. After the substitution of $\bar{U}(\bar{z}, \bar{t})$ into Eq. (61), the first term of Eq. (61) will take the form of

$$\begin{aligned} &\frac{1}{(\beta_m)^{1/2}} \int_0^{\bar{d}} \sigma(\bar{z}) \frac{\partial \bar{U}}{\partial \bar{t}} \psi_m(\bar{z}) d\bar{z} \\ &\quad = \frac{1}{(\beta_m)^{1/2}} \int_0^{\bar{d}} \sigma(\bar{z}) \frac{\partial}{\partial \bar{t}} \left[\sum_{r=1}^{M} \tau_r(\bar{t}) \frac{\psi_r(\bar{z})}{(\beta_r)^{1/2}} \right] \psi_m(\bar{z}) d\bar{z} \end{aligned} \tag{63}$$

By rearranging the summation and differential operators on the right-hand side of Eq. (63) and substituting the expression for ψ_m from Eq. (56), we obtain

$$\begin{aligned} &\frac{1}{(\beta_m)^{1/2}} \int_0^{\bar{d}} \sigma(\bar{z}) \frac{\partial \bar{U}}{\partial \bar{t}} \psi_m(\bar{z}) d\bar{z} \\ &\quad = \sum_{r=1}^{M} \frac{d\tau_r}{d\bar{t}} \int_0^{\bar{d}} \sigma(\bar{z}) \frac{\sin(N_r \bar{z})}{(\beta_r)^{1/2}} \frac{\sin(N_m \bar{z})}{(\beta_m)^{1/2}} d\bar{z} \end{aligned} \tag{64}$$

The integral term in the RHS of the equation, denoted as D_{mr}, is an $M \times M$ square matrix and can be expressed as

$$D_{mr} = \int_0^{\bar{d}} \sigma(\bar{z}) \frac{\sin(N_r \bar{z})}{(\beta_r)^{1/2}} \frac{\sin(N_m \bar{z})}{(\beta_m)^{1/2}} d\bar{z} \tag{65}$$

Substituting the definition of $\sigma(\bar{z})$ from Eq. (32) into the equation and subsequently splitting the integration limits for each soil layer results in

$$D_{mr} = \sum_{i=1}^{N} \sigma_i \int_{\bar{d}_{i-1}}^{\bar{d}_i} \frac{\sin(N_r \bar{z})}{(\beta_r)^{1/2}} \frac{\sin(N_m \bar{z})}{(\beta_m)^{1/2}} d\bar{z} \tag{66}$$

where, $\bar{d}_0$ and $\bar{d}_N$ represents $\bar{z} = 0$ and $\bar{z} = \bar{d}$, respectively.

Eq. (64) can now be reformulated using Eq. (65) as

$$\frac{1}{(\beta_m)^{1/2}} \int_0^{\bar{d}} \sigma(\bar{z}) \frac{\partial \bar{U}}{\partial \bar{t}} \psi_m(\bar{z}) d\bar{z} = \sum_{r=1}^{M} D_{mr} \frac{d\tau_r}{d\bar{t}} \tag{67}$$

Eq. (67) clearly establishes the equivalence between the first terms of Eqs. (61) and (62). The next step is to verify the equivalence of their second terms. This is accomplished by first applying integration by parts to the second term of Eq. (61), as given by

$$\begin{aligned} &\frac{1}{(\beta_m)^{1/2}} \int_0^{\bar{d}} \left\{ -\frac{\partial}{\partial \bar{z}} \left[\omega(\bar{z}) \frac{\partial \bar{U}}{\partial \bar{z}} \right] + \frac{\partial \bar{U}}{\partial \bar{z}} \right\} \psi_m(\bar{z}) d\bar{z} \\ &\quad = \frac{1}{(\beta_m)^{1/2}} \left\{ \left[-\omega(\bar{z}) \frac{\partial \bar{U}}{\partial \bar{z}} + \bar{U} \right]_0^{\bar{d}} \times \psi_m|_0^{\bar{d}} \right. \\ &\qquad \left. - \int_0^{\bar{d}} \left[-\omega(\bar{z}) \frac{\partial \bar{U}}{\partial \bar{z}} + \bar{U} \right] \frac{d\psi_m}{dz} d\bar{z} \right\} \end{aligned} \tag{68}$$

Given that $\psi_m(\bar{z})$ satisfies homogeneous boundary conditions at the edge boundaries, as evident from Eq. (56), which implies $\psi_m|_0^{\bar{d}} = 0$, Eq. (68) can therefore be rewritten as

$$\begin{aligned} &\frac{1}{(\beta_m)^{1/2}} \int_0^{\bar{d}} \left\{ -\frac{\partial}{\partial \bar{z}} \left[\omega(\bar{z}) \frac{\partial \bar{U}}{\partial \bar{z}} \right] + \frac{\partial \bar{U}}{\partial \bar{z}} \right\} \psi_m(\bar{z}) d\bar{z} \\ &\quad = \frac{1}{(\beta_m)^{1/2}} \left\{ - \int_0^{\bar{d}} \left[-\omega(\bar{z}) \frac{\partial \bar{U}}{\partial \bar{z}} + \bar{U} \right] \frac{d\psi_m}{dz} d\bar{z} \right\} \end{aligned} \tag{69}$$

It is important to note that the right-hand side of Eq. (69) reduces to a weak form since the differentiability requirement of $\omega(\bar{z})$ is relaxed due to integration. Given that $\omega(\bar{z})$ is a piecewise continuous function, as defined in Eq. (31), transforming the original equation into its weak form effectively addresses the challenge of dealing with the derivative of a piecewise continuous function.

The next step is to substitute the expression for $\bar{U}(\bar{z}, \bar{t})$ into the right-hand side of Eq. (69), resulting in

$$\begin{aligned} &\frac{1}{(\beta_m)^{1/2}} \int_0^{\bar{d}} \left\{ -\frac{\partial}{\partial \bar{z}} \left[\omega(\bar{z}) \frac{\partial \bar{U}}{\partial \bar{z}} \right] + \frac{\partial \bar{U}}{\partial \bar{z}} \right\} \psi_m(\bar{z}) d\bar{z} \\ &\quad = \frac{1}{(\beta_m)^{1/2}} \left\{ \int_0^{\bar{d}} \omega(\bar{z}) \frac{\partial}{\partial \bar{z}} \left[\sum_{r=1}^{M} \tau_r(\bar{t}) \frac{\psi_r(\bar{z})}{(\beta_r)^{1/2}} \right] \frac{d\psi_m}{dz} d\bar{z} \right. \\ &\qquad \left. - \int_0^{\bar{d}} \left[\sum_{r=1}^{M} \tau_r(\bar{t}) \frac{\psi_r(\bar{z})}{(\beta_r)^{1/2}} \right] \frac{d\psi_m}{dz} d\bar{z} \right\} \end{aligned} \tag{70}$$

Rearranging the summation and differential operators on the right-hand side of Eq. (70) and substituting the expression for ψ_m from Eq. (56), we obtain

$$\begin{aligned} &\frac{1}{(\beta_m)^{1/2}} \int_0^{\bar{d}} \left\{ -\frac{\partial}{\partial \bar{z}} \left[\omega(\bar{z}) \frac{\partial \bar{U}}{\partial \bar{z}} \right] + \frac{\partial \bar{U}}{\partial \bar{z}} \right\} \psi_m(\bar{z}) d\bar{z} \\ &\quad = \sum_{r=1}^{M} \tau_r(\bar{t}) \left\{ \int_0^{\bar{d}} \omega(\bar{z}) N_r N_m \frac{\cos(N_r \bar{z}) \cos(N_m \bar{z})}{(\beta_r)^{1/2} (\beta_m)^{1/2}} d\bar{z} \right. \\ &\qquad \left. - \int_0^{\bar{d}} N_m \frac{\sin(N_r \bar{z}) \cos(N_m \bar{z})}{(\beta_r)^{1/2} (\beta_m)^{1/2}} d\bar{z} \right\} \end{aligned} \tag{71}$$

The integral term on the right-hand side of the above equation is represented by E_{mr}, which is an $M \times M$ square matrix and can be expressed as

$$E_{mr} = \int_0^{\bar{d}} \omega(\bar{z}) N_r N_m \frac{\cos(N_r \bar{z}) \cos(N_m \bar{z})}{(\beta_r)^{1/2} (\beta_m)^{1/2}} d\bar{z} - \int_0^{\bar{d}} N_m \frac{\sin(N_r \bar{z}) \cos(N_m \bar{z})}{(\beta_r)^{1/2} (\beta_m)^{1/2}} d\bar{z} \tag{72}$$

By substituting the definition of $\omega(\bar{z})$ from Eq. (31) into the equation and then dividing the integration limits for each individual soil layer, we obtain

$$E_{mr} = \sum_{i=1}^{N} \omega_i \int_{\bar{d}_{i-1}}^{\bar{d}_i} N_r N_m \frac{\cos(N_r \bar{z}) \cos(N_m \bar{z})}{(\beta_r)^{1/2} (\beta_m)^{1/2}} d\bar{z} - \int_0^{\bar{d}} N_m \frac{\sin(N_r \bar{z}) \cos(N_m \bar{z})}{(\beta_r)^{1/2} (\beta_m)^{1/2}} d\bar{z} \tag{73}$$

Therefore, Eq. (71) can now be rewritten using Eq. (72) as

$$\frac{1}{(\beta_m)^{1/2}} \int_0^{\bar{d}} \left\{ -\frac{\partial}{\partial \bar{z}} \left[\omega(\bar{z}) \frac{\partial \bar{U}}{\partial \bar{z}} \right] + \frac{\partial \bar{U}}{\partial \bar{z}} \right\} \psi_m(\bar{z}) d\bar{z} = \sum_{r=1}^{M} E_{mr} \tau_r(\bar{t}) \tag{74}$$

The final step involves establishing the interrelationship between the RHS term of Eqs. (61) and (62). This is achieved by incorporating the function definitions of $\sigma(\bar{z})$, $\bar{T}_{st}$, and $\psi_m(\bar{z})$ as given in Eqs. (32), (50), and (56), respectively, into the equation, which results in

$$-\frac{1}{(\beta_m)^{1/2}} \int_0^{\bar{d}} \sigma(\bar{z}) \frac{\partial \bar{T}_{st}}{\partial \bar{t}} \psi_m(\bar{z}) d\bar{z} = -\sum_{i=1}^{N} \sigma_i \int_{\bar{d}_{i-1}}^{\bar{d}_i} \left[\frac{dP_i}{dt} + \frac{dQ_i}{dt} \exp\left(\frac{\bar{z}}{\omega_i} \right) \right] \frac{\sin(N_m \bar{z})}{(\beta_m)^{1/2}} d\bar{z} \tag{75}$$

where P_i and Q_i = functions of the transient top boundary $\bar{T}_T(\bar{t})$, as defined in Eqs. (51)–(54).

The integral term on the right-hand side of the equation is represented by F_m, which is an $M \times 1$ column matrix and can be expressed as

$$-\sum_{i=1}^{N} \sigma_i \int_{\bar{d}_{i-1}}^{\bar{d}_i} \left[\frac{dP_i}{dt} + \frac{dQ_i}{dt} \exp\left(\frac{\bar{z}}{\omega_i} \right) \right] \frac{\sin(N_m \bar{z})}{(\beta_m)^{1/2}} d\bar{z} = F_m(\bar{t}) \tag{76}$$

Thus, Eqs. (75) and (76) demonstrate the equivalence of the RHS terms in Eqs. (61) and (62). Finally, Eq. (62) in concise (matrix) form is written as

$$\mathbf{D} \frac{d\boldsymbol{\tau}(\bar{t})}{d\bar{t}} + \mathbf{E} \boldsymbol{\tau}(\bar{t}) = \mathbf{F}(\bar{t}) \tag{77}$$

Operating $\mathbf{D}^{-1}$ matrix on both sides of Eq. (77) gives

$$\frac{d\boldsymbol{\tau}(\bar{t})}{d\bar{t}} + \mathbf{D}^{-1} \mathbf{E} \boldsymbol{\tau}(\bar{t}) = \mathbf{D}^{-1} \mathbf{F}(\bar{t}) \tag{78}$$

Multiplying Eq. (78) by $\exp(\mathbf{D}^{-1}\mathbf{E}\bar{t})$ on both sides and then integrating with respect to $\bar{t}$ over the range $[0, \bar{t}]$ gives (Sarmah et al. 2020)

$$\boldsymbol{\tau}(\bar{t}) = \exp(-\mathbf{D}^{-1}\mathbf{E}\bar{t}) \boldsymbol{\tau}(0) + \exp(-\mathbf{D}^{-1}\mathbf{E}\bar{t}) \int_0^{\bar{t}} \exp(\mathbf{D}^{-1}\mathbf{E}\bar{t}) \mathbf{D}^{-1} \mathbf{F}(\bar{t}) d\bar{t} \tag{79}$$

The matrix exponential, $\exp(-\mathbf{D}^{-1}\mathbf{E}\bar{t})$, appearing in Eq. (79) is computed using MATLAB. It is important to be noted that $\boldsymbol{\tau}(0)$ in the equation corresponds to the GITT coefficients τ_m at $\bar{t} = 0$. Thus, $\boldsymbol{\tau}(0)$ is determined by applying the initial condition given in Eq. (30), leading to

$$\bar{U}(\bar{z}, 0) = \sum_{m=1}^{M} \tau_m(0) \frac{\sin(N_m \bar{z})}{(\beta_m)^{1/2}} = \bar{T}_r(\bar{z}) - \bar{T}_{st}(\bar{z}, 0) \tag{80}$$

It should be noted that $\bar{T}_r(\bar{z})$ and $\bar{T}_{st}(\bar{z}, 0)$ are identical. $\bar{T}_r(\bar{z})$ represents the initial condition of the heat flow problem, whose analytical expression is derived considering the top boundary as a constant temperature profile with $\bar{T}_T = 1$. On the other hand, $\bar{T}_{st}(\bar{z}, 0)$ also represents the steady-state temperature distribution in the flow domain, where the top boundary corresponds to the initial temperature. This equivalence can be established by setting $\bar{t} = 0$ in Eq. (12), which gives $\bar{T}_T(0) = 1$. Consequently,

$$\sum_{m=1}^{M} \tau_m(0) \frac{\sin(N_m \bar{z})}{(\beta_m)^{1/2}} = 0 \Rightarrow \tau_m(0) = 0 \tag{81}$$

The unknown coefficient $\tau_m(\bar{t})$, determined from Eq. (79), is then substituted into Eq. (36) to evaluate the function $\bar{U}(\bar{z}, \bar{t})$. Finally, $\bar{U}(\bar{z}, \bar{t})$, along with $\bar{T}_{st}(\bar{z}, \bar{t})$, is incorporated into Eq. (15) to obtain the desired dimensionless transient temperature distribution in the layered soil subjected to a time-dependent temperature boundary.

Data Availability Statement

Some or all data, models, or codes that support the findings of this study are available from the corresponding author upon reasonable request.

Author Contributions

Vishal Bashist: Formal analysis; Methodology; Software; Validation; Visualization; Writing – original draft. Ratan Sarmah: Conceptualization; Formal analysis; Methodology; Supervision; Visualization; Writing – review and editing. Ickkshaanshu Sonkar: Formal analysis; Methodology; Supervision; Visualization; Writing – review and editing.

References

Aryeni, T., and V. Ginting. 2022. "A semi-analytical solution of Richards equation for two-layered one-dimensional soil." *Adv. Water Resour.* 165 (Jul): 104199. https://doi.org/10.1016/j.advwatres.2022.104199.

Baek, J. Y., B. H. Park, G. C. Rau, and K. K. Lee. 2022. "Experimental evidence for local thermal non-equilibrium during heat transport in sand representative of natural conditions." *J. Hydrol.* 608 (Aug): 127589. https://doi.org/10.1016/j.jhydrol.2022.127589.

Bakker, M., R. Caljé, F. Schaars, K. J. Van Der Made, and S. De Haas. 2015. "An active heat tracer experiment to determine groundwater velocities using fiber optic cables installed with direct push equipment." *Water Resour. Res.* 51 (4): 2760–2772. https://doi.org/10.1002/2014WR016632.

Bekele, E., B. Patterson, S. Toze, A. Furness, S. Higginson, and M. Shackleton. 2014. "Aquifer residence times for recycled water estimated using chemical tracers and the propagation of temperature signals at a managed aquifer recharge site in Australia Elise." *Hydrogeol. J.* 22 (6): 1383–1401. https://doi.org/10.1007/s10040-014-1142-0.

Bense, V. F., and B. L. Kurylyk. 2017. "Tracking the subsurface signal of decadal climate warming to quantify vertical groundwater flow rates." *Geophys. Res. Lett.* 44 (24): 12244–12253. https://doi.org/10.1002/2017GL076015.

Bredehoeft, J. D., and I. S. Papaopulos. 1965. "Rates of vertical groundwater movement estimated from the Earth's thermal profile." *Water Resour. Res.* 1 (2): 325–328. https://doi.org/10.1029/WR001i002p00325.

Chang, C. H., Y. F. Lin, Y. J. Shiau, Y. Z. Tsai, and J. P. Tsai. 2023. "Effects of soil type and thermal boundary on predicting temperature profiles and groundwater fluxes." *Ground Water* 61 (2): 203–214. https://doi.org/10.1111/gwat.13295.

Chang, C. H., and J. P. Tsai. 2021. "Analysis of the heat transfer in subsurface porous media with considering Robin-type boundaries and arbitrary surface temperature variations." *Int. J. Heat Mass Transfer* 173 (Jul): 121222. https://doi.org/10.1016/j.ijheatmasstransfer.2021.121222.

Cotta, R. M., K. M. Lisboa, and J. L. Z. Zotin. 2020. "Integral transforms for flow and transport in discrete and continuum models of fractured heterogeneous porous media." *Adv. Water Resour.* 142 (Aug): 103621. https://doi.org/10.1016/j.advwatres.2020.103621.

Deng, B., J. Li, B. Zhang, and N. Li. 2014. "Integral transform solution for solute transport in multi-layered porous media with the implicit treatment of the interface conditions and arbitrary boundary conditions." *J. Hydrol.* 517 (Sep): 566–573. https://doi.org/10.1016/j.jhydrol.2014.05.072.

Doro, K. O., O. A. Cirpka, and C. Leven. 2015. "Tracer tomography: Design concepts and field experiments using heat as a tracer." Supplement, *Ground Water* 53 (S1): 139–148. https://doi.org/10.1111/gwat.12299.

Farthing, M. W., and F. L. Ogden. 2017. "Numerical solution of Richards' equation: A review of advances and challenges." *Soil Sci. Soc. Am. J.* 81 (6): 1257–1269. https://doi.org/10.2136/sssaj2017.02.0058.

Gabrielsson, A., M. Lehtmets, L. Moritz, and U. Bergdahl. 1997. *Heat storage in soft clay: Field tests with heating and freezing of the soil*. Linköping, Sweden: Swedish Geotechnical Institute.

Haberman, R. 2013. *Applied partial differential equations with fourier series and boundary value problems*. 5th ed. London: Pearson.

Haji-Sheikh, A., J. V. Beck, and D. Agonafer. 2003. "Steady-state heat conduction in multi-layer bodies." *Int. J. Heat Mass Transfer* 46 (13): 2363–2379. https://doi.org/10.1016/S0017-9310(02)00542-2.

Harris, R. N., and D. S. Chapman. 1995. "Climate change on the Colorado Plateau of eastern Utah inferred from borehole temperatures." *J. Geophys. Res.* 100 (B4): 6367–6381. https://doi.org/10.1029/94JB02165.

Irvine, D. J., I. Cartwright, V. E. A. Post, C. T. Simmons, and E. W. Banks. 2016. "Uncertainties in vertical groundwater fluxes from 1-D steady state heat transport analyses caused by heterogeneity, multidimensional flow, and climate change Dylan." *Water Resour. Res.* 52 (2): 813–826. https://doi.org/10.1002/2015WR017702.

Kampen, V. R., U. Schneidewind, C. Anibas, A. Bertagnoli, D. Tonina, G. Vandersteen, C. Luce, S. Krause, and M. van Berkel. 2022. "LPMLEn–A frequency domain method to estimate vertical streambed fluxes and sediment thermal properties in semi-infinite and bounded domains." *Water Resour. Res.* 58 (3): 1–13. https://doi.org/10.1029/2021WR030886.

Klepikova, M., S. Wildemeersch, T. Hermans, P. Jamin, P. Orban, F. Nguyen, S. Brouyère, and A. Dassargues. 2016. "Heat tracer test in an alluvial aquifer: Field experiment and inverse modelling." *J. Hydrol.* 540 (Sep): 812–823. https://doi.org/10.1016/j.jhydrol.2016.06.066.

Koch, F. W., E. B. Voytek, F. D. Day-Lewis, R. Healy, M. A. Briggs, J. W. Lane, and D. Werkema. 2016. "1DTempPro V2: New features for inferring groundwater/surface-water exchange." *Ground Water* 54 (3): 434–439. https://doi.org/10.1111/gwat.12369.

Kothawale, D. R., and H. N. Singh. 2017. "Recent trends in tropospheric temperature over India during the period 1971–2015." *Earth Space Sci.* 4 (5): 240–246. https://doi.org/10.1002/2016EA000246.

Kumar, A., I. Sonkar, and R. Sarmah. 2024. "Modeling root zone water and salt transport using matric flux potential based root water uptake distribution." *J. Hydrol.* 630 (Nov): 130712. https://doi.org/10.1016/j.jhydrol.2024.130712.

Kumar, R., J. Kuttippurath, G. S. Gopikrishnan, P. Kumar, and H. Varikoden. 2023. "Enhanced surface temperature over India during 1980–2020 and future projections: Causal links of the drivers and trends." *npj Clim. Atmos. Sci.* 6 (1): 164. https://doi.org/10.1038/s41612-023-00494-0.

Kurylyk, B. L., and D. J. Irvine. 2016. "Analytical solution and computer program (FAST)to estimate fluid fluxes from subsurface temperature profiles." *Water Resour. Res.* 5 (2): 725–733. https://doi.org/10.1002/2015WR017990.

Kurylyk, B. L., D. J. Irvine, and V. F. Bense. 2018. "Theory, tools, and multidisciplinary applications for tracing groundwater fluxes from temperature profiles." *Wiley Interdiscip. Rev.: Water* 6 (1): e1329. https://doi.org/10.1002/wat2.1329.

Kurylyk, B. L., D. J. Irvine, S. Carey, M. A. Briggs, D. Werkema, and M. Bonham. 2017a. *Streambed temperature data for the manuscript: Heat as a hydrologic tracer in shallow and deep heterogeneous media: Analytical solution, spreadsheet tool, and field applications: US Geological Survey data release*. Washington, DC: USGS. https://doi.org/10.5066/F7NZ85VG.

Kurylyk, B. L., D. J. Irvine, S. K. Carey, M. A. Briggs, D. D. Werkema, and M. Bonham. 2017b. "Heat as a groundwater tracer in shallow and deep heterogeneous media: Analytical solution, spreadsheet tool, and field applications." *Hydrol. Process.* 31 (14): 2648–2661. https://doi.org/10.1002/hyp.11216.

Kurylyk, B. L., and K. T. B. Macquarrie. 2013. "A new analytical solution for assessing climate change impacts on subsurface temperature." *Hydrol. Process.* 28 (7): 3161–3172. https://doi.org/10.1002/hyp.9861.

LeRoux, N. K., B. L. Kurylyk, M. A. Briggs, D. J. Irvine, J. J. Tamborski, and V. F. Bense. 2021. "Using heat to trace vertical water fluxes in sediment experiencing concurrent tidal pumping and groundwater discharge." *Water Resour. Res.* 57 (2): 1–13. https://doi.org/10.1029/2020WR027904.

Lin, Y. F., C. H. Chang, and J. P. Tsai. 2022. "Analytical solution for estimating transient vertical groundwater flux from temperature-depth profiles." *J. Hydrol.* 610 (Apr): 127920. https://doi.org/10.1016/j.jhydrol.2022.127920.

Liu, C., J. E. Szecsody, J. M. Zachara, and W. P. Ball. 2000. "Use of the generalized integral transform method for solving equations of solute transport in porous media." *Adv. Water Resour.* 23 (5): 483–492. https://doi.org/10.1016/S0309-1708(99)00048-2.

Liu, G., and B. C. Si. 2008. "Analytical modeling of one-dimensional diffusion in layered systems with position-dependent diffusion coefficients." *Adv. Water Resour.* 31 (2): 251–268. https://doi.org/10.1016/j.advwatres.2007.08.008.

Liu, Q., S. Chen, and B. Zhou. 2024. "Estimating temporal patterns of vertical groundwater flux using multidepth temperature time series: A numerical method." *J. Hydrol.* 639 (1): 131623. https://doi.org/10.1016/j.jhydrol.2024.131623.

McCallum, A. M., M. S. Andersen, G. C. Rau, and R. I. Acworth. 2012. "A 1-D analytical method for estimating surface water-groundwater interactions and effective thermal diffusivity using temperature time series." *Water Resour. Res.* 48 (11): W11532. https://doi.org/10.1029/2012WR012007.

Mikhailov, M. D., and M. N. Ozisik. 1984. *Unified analysis and solutions of heat and mass diffusion*. New York: Dover Publications.

Piskunov, N. 1974. Vol. II of *A solution manual for differential and integral calculus*. Moscow: Mir Publishers.

Rezaei, M., P. Seuntjens, I. Joris, W. Boënne, S. Van Hoey, P. Campling, and W. M. Cornelis. 2016. "Sensitivity of water stress in a two-layered sandy grassland soil to variations in groundwater depth and soil hydraulic parameters." *Hydrol. Earth Syst. Sci.* 20 (1): 487–503. https://doi.org/10.5194/hess-20-487-2016.

Sarmah, R., and G. Barua. 2015. "Hydraulics of a partially penetrating ditch drainage system in a layered soil receiving water from a ponded field." *J. Irrig. Drain. Eng.* 141 (8): 04015001. https://doi.org/10.1061/(ASCE)IR.1943-4774.0000861.

Sarmah, R., G. Barua, and S. A. Kartha. 2020. "Experimental and analytical investigation of ponded ditch drainage system with temporal boundaries." *J. Hydrol. Eng.* 25 (12): 1–11. https://doi.org/10.1061/(ASCE)HE.1943-5584.0002012.

Sarmah, R., I. Sonkar, and S. R. Chavan. 2022. "Analytical solutions for predicting seepage in a layered ditch drainage system under Dirichlet and lagging Robin boundary conditions." *Hydrol. Sci. J.* 67 (13): 1917–1940. https://doi.org/10.1080/02626667.2022.2101891.

Scarborough, J. B. 1966. *Numerical mathematical analysis*. New Delhi, India: Oxford & IBH.

Shan, C., and G. Bodvarsson. 2004. "An analytical solution for estimating percolation rate by fitting temperature profiles in the vadose zone." *J. Contam. Hydrol.* 68 (1–2): 83–95. https://doi.org/10.1016/S0169-7722(03)00126-8.

Shi, W., and Q. Wang. 2023. "An analytical model of multi-layered heat transport to estimate vertical streambed fluxes and sediment thermal properties." *J. Hydrol.* 625 (PA): 129963. https://doi.org/10.1016/j.jhydrol.2023.129963.

Simon, N., and O. Bour. 2023. "An ADTS toolbox for automatically interpreting active distributed temperature sensing measurements." *Ground Water* 61 (2): 215–223. https://doi.org/10.1111/gwat.13172.

Singh, A., V. Bejagam, and A. Sharma. 2024. "Investigating the role of groundwater in ecosystem water use efficiency in India considering irrigation, climate and land use." *Groundwater Sustainable Dev.* 27 (Nov): 101363. https://doi.org/10.1016/j.gsd.2024.101363.

Stallman, R. W. 1965. "Steady one-dimensional fluid flow in a semi-infinite porous medium with sinusoidal surface temperature." *J. Geophys. Res.* 70 (12): 2821–2827. https://doi.org/10.1029/JZ070i012p02821.

Suzuki, S. 1960. "Percolation measurements based on heat flow through soil with special reference to paddy fields." *J. Geophys. Res.* 65 (9): 2883–2885. https://doi.org/10.1029/JZ065i009p02883.

Taniguchi, M., J. Shimada, T. Tanaka, I. Kayane, Y. Sakura, Y. Shimano, S. Dapaah-Siakwan, and S. Kawashima. 1999. "Disturbances of temperature-depth profiles due to surface climate change and subsurface water flow: 1. An effect of linear increase in surface temperature caused by global warming and urbanization in the Tokyo metropolitan area, Japan." *Water Resour. Res.* 35 (5): 1507–1517. https://doi.org/10.1029/1999WR900009.

Wagner, V., T. Li, P. Bayer, C. Leven, P. Dietrich, and P. Blum. 2014. "Thermal tracer testing in a sedimentary aquifer: Field experiment (Lauswiesen, Germany) and numerical simulation Valentin." *Hydrogeol. J.* 22 (1): 175–187. https://doi.org/10.1007/s10040-013-1059-z.

Zhou, R., and Q. Wang. 2022. "Analytical model for heat transfer in a discrete parallel fracture–rock matrix system." *Ground Water* 61 (2): 183–192. https://doi.org/10.1111/gwat.13174.